

# Protoplanetary Disk Structures in Ophiuchus

Sean M. Andrews<sup>1,2</sup>, D. J. Wilner<sup>1</sup>, A. M. Hughes<sup>1</sup>, Chunhua Qi<sup>1</sup>, and C. P. Dullemond<sup>3</sup>

## ABSTRACT

We present the results of a high angular resolution ( $0''.3 \approx 40$  AU) Submillimeter Array survey of the 345 GHz ( $870 \mu\text{m}$ ) thermal continuum emission from 9 of the brightest, and therefore most massive, circumstellar disks in the  $\sim 1$  Myr-old Ophiuchus star-forming region. Using two-dimensional radiative transfer calculations, we simultaneously fit the observed continuum visibilities and broadband spectral energy distribution for each disk with a parametric structure model. Compared to previous millimeter studies, this survey includes significant upgrades in modeling, data quality, and angular resolution that provide improved constraints on key structure parameters, particularly those that characterize the spatial distribution of mass in the disks. In the context of a surface density profile motivated by similarity solutions for viscous accretion disks,  $\Sigma \propto (R/R_c)^{-\gamma} \exp[-(R/R_c)^{2-\gamma}]$ , the best-fit models for the sample disks have characteristic radii  $R_c \approx 20$ -200 AU, high disk masses  $M_d \approx 0.005$ - $0.14 M_\odot$  (a sample selection bias), and a narrow range of radial  $\Sigma$  gradients ( $\gamma \approx 0.4$ - $1.0$ ) around a median  $\gamma = 0.9$ . These density structures are used in conjunction with accretion rate estimates from the literature to help characterize the viscous evolution of the disk material. Using the standard prescription for disk viscosities, those combined constraints indicate that  $\alpha \approx 0.0005$ - $0.08$ . Three of the sample disks show large ( $R \approx 20$ - $40$  AU) central cavities in their continuum emission morphologies, marking extensive zones where dust has been physically removed and/or has significantly diminished opacities. Based on the current requirements of planet formation models, these emission cavities and the structure constraints for the sample as a whole suggest that these young disks may eventually produce planetary systems, and have perhaps already started.

*Subject headings:* accretion, accretion disks — circumstellar matter — planetary systems: protoplanetary disks — solar system: formation — stars: pre-main-sequence

---

<sup>1</sup>Harvard-Smithsonian Center for Astrophysics, 60 Garden Street, Cambridge, MA 02138; sandrews, dwilner, mhughes, cqi@cfa.harvard.edu

<sup>2</sup>Hubble Fellow

<sup>3</sup>Max Planck Institut für Astronomie, Königstuhl 17, 69117 Heidelberg, Germany; dullemon@mpia.de

## 1. Introduction

Within a span of  $\sim 10$  Myr, the material in a circumstellar disk will either be accreted onto its star, dispersed into the interstellar medium, or incorporated into the larger bodies of a burgeoning planetary system. Throughout that time, viscous and gravitational forces spatially redistribute this material and its angular momentum, driving a net inward mass flow that can accrete onto the stellar surface (e.g., Pringle 1981). Meanwhile, dust grains settle to the disk midplane and accumulate into larger solid bodies (Beckwith et al. 2000; Dullemond & Dominik 2005). If that growth progresses sufficiently, those bodies can dynamically influence the remaining disk material through accretion, ejection, and the sculpting of gaps and large-scale cavities (Lin & Papaloizou 1993; Papaloizou et al. 2007). Toward the end of the disk lifetime, winds driven by energetic radiation from the central star can rapidly sweep any remaining material into the local environment (Clarke et al. 2001; Alexander et al. 2006; Alexander & Armitage 2007). Each of these evolutionary mechanisms is critically influenced by the spatial mass distribution – the density structure – of the disk material.

While the theoretical machinery behind these evolution processes has been developed in some detail (see Dullemond et al. 2007; Youdin 2008; Alexander 2008), empirical constraints on densities in circumstellar disks are still notably rare. Observational limitations are largely to blame, in part due to the small angles that disks subtend on the sky and the inability to directly observe the dominant mass constituent (molecular hydrogen). In light of these deficiencies, many studies use a crude approximation of the primordial solar disk (the Minimum Mass Solar Nebula, or MMSN) as a reference point. A surface density profile ( $\Sigma$ ) for the MMSN is constructed by augmenting the current planet masses to match solar abundances, and then smearing those masses into concentric annuli. The result is usually fit with a radial power-law,  $\Sigma \propto R^{-3/2}$  (e.g., Weidenschilling 1977; Hayashi 1981). Spatially resolved observations of the dust in disks around nearby young stars can provide more direct constraints on a potentially wide variety of density structures. Measurements at millimeter wavelengths are particularly desirable, as the thermal continuum emission from dust grains is optically thin and therefore probes the full disk volume (Beckwith et al. 1990; Beckwith & Sargent 1991). For a simple prescription of that emission,  $S_\nu \propto B_\nu(1 - e^{-\tau})$ , where  $S_\nu$  is the surface brightness,  $B_\nu$  the Planck function at the local temperature ( $T$ ), and  $\tau$  the optical depth. The low millimeter optical depths simplify the reprocessing term ( $1 - e^{-\tau} \approx \tau$ ) and imply that the emission is produced near the cold disk midplane. Assuming the Rayleigh-Jeans approximation is valid ( $B_\nu \propto T$ ) and defining the optical depth as the product of the dust opacity and column (surface) density ( $\tau = \kappa\Sigma$ ), we note that the millimeter continuum emission tracks a compound product of physical conditions in the disk,  $S_\nu \propto \kappa\Sigma T$ .

Although associating the emission and disk structure in this way is simplistic, it has served as the intuitive basis for interpreting a wealth of millimeter observations. With some disk-averaged assumptions for  $\kappa$  and  $T$ , it has been used to estimate hundreds of disk masses from single-dish millimeter photometry surveys (Beckwith et al. 1990; André & Montmerle 1994; Osterloh & Beckwith 1995; Andrews & Williams 2005, 2007b). Interferometric studies have typically taken a more sophisticated approach and fitted resolved millimeter data with parametric disk structure models,

where  $\Sigma \propto R^{-p}$ . A wide variety of surface density profiles, with  $p$  values ranging from 0 to 2, have been derived from such fits, based on the millimeter continuum data alone (Lay et al. 1994, 1997; Mundy et al. 1996) or in combination with the broadband spectral energy distribution (SED; Wilner et al. 2000; Testi et al. 2001; Akeson et al. 2002; Kitamura et al. 2002; Andrews & Williams 2007a). Similar results have been determined from resolved spectral images of line emission from trace molecular species, which suffer from the additional complexities of excitation and abundance variations (Dutrey et al. 1998, 2003; Guilloteau & Dutrey 1998; Guilloteau et al. 1999; Simon et al. 2000; Dartois et al. 2003; Piétu et al. 2003, 2007; Isella et al. 2007).

While those studies have profoundly shaped our knowledge of disk structure, they are all fundamentally limited by low angular resolution. Typical interferometer baselines probed angular scales down to 1-4'', corresponding to 125-500 AU for the nearest star-forming regions. With disk diameters in the 100-1000 AU range, these previous observations simply did not have the spatial dynamic range required to accurately characterize disk emission morphologies, and therefore disk structures. For such limited angular resolution, the emission could only be probed at large disk radii ( $R \geq 60$  AU at best), well outside the region where the density structure is most relevant to the viscous evolution and planet formation processes ( $R \leq 40$  AU). Some recent studies have overcome these restrictions with long interferometer baselines and provided the first millimeter-wave views of structure in the inner disk ( $R \approx 20$ -50 AU) with sub-arcsecond resolution images (0.3-0.5''; Hamidouche et al. 2006; Piétu et al. 2006; Guilloteau et al. 2008; Andrews et al. 2008). A few such observations have even discovered large central cavities in the dust emission – potential signatures of young planetary systems (Piétu et al. 2006; Brown et al. 2008, 2009; Hughes et al. 2007, 2009). These novel high angular resolution capabilities offer new insights on disk structures that can help refine our understanding of both disk evolution and planet formation.

With those goals in mind, we present the results of a new high angular resolution (0'3) survey of the 345 GHz (870  $\mu$ m) continuum emission from 9 circumstellar disks in the  $\sim$ 1 Myr-old Ophiuchus star formation region. We use these data to extract constraints on the disk structures in the spirit of the study by Andrews & Williams (2007a), but now with major improvements in the data quality, spatial resolution, and modeling techniques. The interferometric survey observations and data calibration are described in §2. Our disk model calculations are introduced in §3, and the resulting constraints on key disk structure parameters are presented in §4. The derived disk structures are examined in the contexts of their viscous properties and planet formation prospects in §5. A summary of our principal conclusions is provided in §6.

## 2. Observations and Data Reduction

A sample of 9 disks was observed with the very extended (V) configuration of the Submillimeter Array interferometer (SMA; Ho et al. 2004) at Mauna Kea, Hawaii. In this array configuration, the eight 6 m SMA antennas span baselines of 68-509 m. Double sideband receivers were tuned to a local oscillator (LO) frequency of 340.755 GHz (880  $\mu$ m). Each sideband contains 24 partially overlapping

104 MHz chunks centered  $\pm 5$  GHz from the LO frequency. Similar observations were also obtained in the sub-compact (S), compact (C), and extended (E) SMA configurations, providing baseline lengths of 6-70 m, 16-70 m, and 28-226 m, respectively. Some of the S, C, and E observations had slightly different receiver tunings and correlator setups in an effort to sample the CO  $J=3-2$  transition on a finer spectral resolution scale. A journal of the SMA observations is provided in Table 1. The C and E data obtained prior to 2007 were already described by Andrews & Williams (2007a). The V data for SR 21 in the SMA archive were originally presented by Brown et al. (2009).

The observing sequence interleaved disk targets and (at least two) quasars in an alternating pattern with a 2:1 integration time ratio. The total cycle time between quasar observations in the V configuration was limited to 8 minutes to ensure that any short-timescale phase variations could be appropriately calibrated. A longer cycle ( $\sim 15$ -20 minutes) was used for the S, C, and E observations. Additional calibrators were observed when the targets were at low elevations ( $< 20^\circ$ ). Depending on their proximity to the disk targets and fluxes at the time of the observations, we chose from a group of four quasars to be used as gain calibrators: J1625–254, J1626–298, J1517–243, and J1733–130. Planets (Uranus, Jupiter, Saturn), satellites (Titan, Callisto), and bright quasars (3C 454.3, 3C 279) were observed as bandpass and absolute flux calibrators depending on their availability and the array configuration. The observing conditions in the V configuration were excellent, with atmospheric opacities  $\leq 0.05$  at 225 GHz (corresponding to  $\leq 1.0$  mm of precipitable water vapor) and well-behaved phase variations on timescales longer than the calibration cycle.

The data were edited and calibrated with the IDL-based MIR software package.<sup>1</sup> The bandpass response was calibrated with observations of a bright planet or quasar, and broadband continuum channels in each sideband were generated by averaging the central 82 MHz in all line-free chunks. The visibility amplitude scale was set based on observations of planets/satellites (Uranus, Titan, or Callisto) and routinely-monitored quasars: the typical systematic uncertainty in the absolute flux scale is  $\sim 10\%$ . The antenna-based complex gain response of the system as a function of time was determined with reference to the quasar nearest on the sky to the corresponding disk target. The other quasar in the observing cycle provides a check on the quality of the phase transfer in the gain calibration process. We find that the millimeter “seeing” generated by atmospheric phase noise and any small baseline errors is minimal,  $0''.1$  at the most. Because the visibilities for all disk targets show excellent agreement between sidebands and on the overlapping baselines for different configurations, all data for a given target were combined. The standard tasks of Fourier inverting the visibilities, deconvolution with the CLEAN algorithm, and restoration with a synthesized beam were conducted with the MIRIAD software package. Maps of the continuum emission were created with a Briggs robust = 0.7 weighting scheme for the visibilities, and maps of the CO  $J=3-2$  line emission were made with natural weighting (robust = 2) for the S, C, and E data when available. Some of the relevant data properties from these synthesized maps are compiled in Table 2.

The synthesized continuum maps for the sample disks are featured together in Figure 1. Each

---

<sup>1</sup>See <http://cfa-www.harvard.edu/~cqi/mircook.html>.

high angular resolution map covers  $4''$  on a side, corresponding to 500 AU at the adopted distance of 125 pc to the Ophiuchus clouds (de Geus et al. 1989; Knude & Høg 1998; Lombardi et al. 2008; Loinard et al. 2008). A centroid position and initial estimate of the viewing geometry of the disk – characterized by the inclination ( $i$ ) and major axis position angle (PA) – were determined by fitting the visibilities with an elliptical Gaussian brightness distribution. Because the continuum emission from the DoAr 44 and SR 21 disks is obviously not centrally peaked, their centroid positions and viewing geometries were estimated by inspection of the images. In most cases, any CO line emission from the disks is significantly contaminated by the local molecular cloud environment. Figure 2 shows CO  $J=3-2$  moment maps for the 3 disks that suffer the least such contamination. Note that the image scale in those panels,  $10''$  (1250 AU) on a side, is significantly larger than for the continuum maps in Figure 1. The contours represent the velocity-integrated intensity (zeroth moment) and the color scale the intensity-weighted velocities (first moment). While CO emission was detected in most cases (except for the SR 21 and WSB 60 data), its association with the disks rather than the molecular cloud is unclear.

### 3. Modeling the Disk Structures

The high angular resolution images exhibited in Figure 1 reveal a striking diversity of continuum emission morphologies, ranging from centrally concentrated and compact (e.g., VSSG 1) to more diffuse and extended (e.g., AS 209) and even cases with large central depressions (SR 21 and DoAr 44). But understanding how the underlying disk structures are related to these morphologies requires a more sophisticated interpretation. Our strategy for this task is to simultaneously reproduce the SMA continuum visibilities and broadband SED for each disk with a parametric structure model. While this is the same concept used in a previous SMA disk survey by Andrews & Williams (2007a), our study makes some major improvements in the model calculations. One critical upgrade is the combined use of a two-dimensional structure model for flared disks and a Monte Carlo radiative transfer code to compute synthetic observations. Rather than the typical *ad hoc* temperature parameterization imposed on such models, the radiative transfer code yields a temperature structure that is internally consistent with a given parametric density structure. These calculations are especially important when fitting a SED, as they provide a proper accounting of emission contributions at each frequency from all of the relevant regions in the disk. In the remainder of this section, we introduce the parametric model for the disk density structures (§3.1), highlight some critical assumptions made in the modeling (§3.2), and explain the radiative transfer calculations (§3.3) and methodology used to estimate model parameters (§3.4).

#### 3.1. The Density Structure Model

The disk structure model and radiative transfer calculations are defined on a spatial grid in spherical coordinates  $\{R, \Theta\}$  ( $150 \times 50$  cells), assuming both azimuthal and mirror (vertically on

either side of the midplane) symmetry. Here,  $\Theta$  is the latitude measured from the pole ( $\Theta = 0$ ) to the equator (the disk midplane,  $\Theta = \pi/2$ ). The grid is linear in the  $\Theta$  dimension, with a fine resolution scale at the midplane and well into the disk atmosphere ( $\Theta \leq 0.5$ ) and coarser sampling near the pole. The grid in the radial dimension is logarithmic, running from an inner edge ( $R_{\text{in}}$ ; see §3.2) to an outer boundary chosen to be large enough to comfortably accommodate all of the disks in this sample (fixed here at 1000 AU, corresponding to  $8''$  projected on the sky).

The two-dimensional density structure in this coordinate system is

$$\rho(R, \Theta) = \frac{\Sigma}{\sqrt{2\pi}Rh} \exp \left[ -\frac{1}{2} \left( \frac{\pi/2 - \Theta}{h} \right)^2 \right], \quad (1)$$

where  $\Sigma$  is the radial surface density profile, and  $h$  is an angular scale height (in latitude). The latter sets the width of the Gaussian vertical density profile, and is taken to be a power-law

$$h = h_c \left( \frac{R}{R_c} \right)^\psi, \quad (2)$$

where  $h_c$  is normalized at a characteristic radius  $R_c$  and  $\psi$  sets the flaring angle of the disk. This angular parameterization is related to a more intuitive physical scale height  $H_R$ , such that

$$H_R \approx Rh = Rh_c \left( \frac{R}{R_c} \right)^\psi = H_c \left( \frac{R}{R_c} \right)^{1+\psi}. \quad (3)$$

We use a generic surface density profile characterized by a power-law in the inner disk and an exponential taper at large radii (see Lynden-Bell & Pringle 1974; Hartmann et al. 1998),

$$\Sigma = \Sigma_c \left( \frac{R}{R_c} \right)^{-\gamma} \exp \left[ -\left( \frac{R}{R_c} \right)^{2-\gamma} \right]. \quad (4)$$

The normalization  $\Sigma_c$  can be written in terms of the total disk mass  $M_d$  by integrating equation (4) over the disk area; when  $\gamma \neq 2$ ,

$$\Sigma_c = (2 - \gamma) \frac{M_d}{2\pi R_c^2}. \quad (5)$$

This prescription for the two-dimensional density structure is fully described by 5 key parameters: the total disk mass ( $M_d$ ), a surface density gradient ( $\gamma$ ), a characteristic radius ( $R_c$ ), a scale height normalization ( $h_c$ ), and a scale height gradient ( $\psi$ ).

Note that by maintaining  $\{h_c, \psi\}$  as free parameters, we do not force the dust distribution to preserve hydrostatic pressure equilibrium in the vertical dimension. For many disks, there is compelling evidence that dust grains have settled toward the disk midplane (Chiang et al. 2001; Dullemond & Dominik 2004b; D’Alessio et al. 2006). Therefore, the dust emission that we use to constrain structure parameters will not necessarily have the same vertical distribution as the gas

(which is expected to be in hydrostatic equilibrium). Some implications of that decision are discussed in §4.1.7. In previous efforts to model disk structure, the surface density profile is assumed to be a power-law,  $\Sigma \propto R^{-p}$ , with a sharp cut-off at an outer boundary,  $R_{\text{out}}$ . However, millimeter observations with improved sensitivity and resolution have shown that this power-law+cut-off behavior yields inconsistent results for the location of  $R_{\text{out}}$ : the optically thin continuum emission indicates a significantly smaller  $R_{\text{out}}$  than the optically thick molecular line emission (Piétu et al. 2005; Isella et al. 2007). Hughes et al. (2008) demonstrated that this discrepancy may be an artifact of the sharp  $\Sigma$  cut-off, and advocated a more gradual density taper at large disk radii. A similar suggestion was made based on optical observations of silhouette disks in Orion (McCaughrean & O’Dell 1996). The  $\Sigma$  profile in equation (4) accommodates these observational findings and is grounded in a mathematical formalism for the viscous evolution of accretion disks (see §5.1).

As Figure 1 illustrates, the disks around SR 21 and DoAr 44 exhibit diminished continuum emission intensities out to sizable distances from the stellar position. We will demonstrate in §4 that the same holds for the WSB 60 disk on slightly smaller radial scales. In these cases, we have modified the surface density profile in equation (4) in an effort to approximately reproduce the observed emission morphologies and SEDs. We define a radius,  $R_{\text{cav}}$ , such that the modified surface density  $\Sigma' = \delta_{\text{cav}}\Sigma$  when  $R \leq R_{\text{cav}}$ , where  $\Sigma$  is taken from equation (4) and  $\delta_{\text{cav}} < 1$  artificially reduces the densities inside the cavity (deficit) in the disk emission.

### 3.2. Fixed Inputs

Various other components of the modeling process are fixed in an effort to keep the problem tractable. Of those fixed inputs, the most important are the properties of the dust grain population and the central star. For the former, we assume a single population of spherical dust grains with a power-law distribution of sizes ( $a$ ), where  $n(a) \propto a^{-3.5}$  from  $a_{\text{min}} = 0.005 \mu\text{m}$  to  $a_{\text{max}} = 1 \text{ mm}$ . D’Alessio et al. (2001) demonstrated that such a large maximum grain size is necessary to account for the millimeter continuum spectra that are typically observed for T Tauri disks (see also Draine 2006). Opacities for this grain population were computed with a Mie scattering code, assuming the silicate and graphite abundances determined for dust grains in the interstellar medium by Draine & Lee (1984) and their updated optical properties as calculated by Weingartner & Draine (2001). At millimeter wavelengths, these opacities ( $\kappa$ ) are similar to the widely-used approximation originally advocated by Beckwith et al. (1990), with  $\kappa \approx 3.5 \text{ cm}^2 \text{ g}^{-1}$  at  $870 \mu\text{m}$  and a spectral index  $\beta \approx 1$  (where  $\kappa_\nu \propto \nu^\beta$  in the relevant frequency range). The opacity spectrum used here is shown in Figure 3, along with the Beckwith et al. (1990) approximation and the Weingartner & Draine (2001) interstellar medium opacities for reference.

As stellar irradiation is the only heating source considered here, the effective temperature ( $T_*$ ) and luminosity ( $L_*$ ) of the central star are fundamental fixed inputs in the models. To determine  $\{T_*, L_*\}$  in a uniform way for each individual target, we first compiled spectral types and foreground extinction estimates from the literature. Using the Kenyon & Hartmann (1995) tabulation, those

spectral classifications were converted to  $T_*$  values. Estimates of  $L_*$  were determined by scaling an appropriate stellar model spectrum (Kurucz 1993; Hauschildt et al. 1999) to match broadband optical photometry (see §4.2 for references) that was de-reddened according to the Mathis (1990) extinction law. For large foreground extinctions ( $A_V \geq 3.5$ ), we used a larger value of the total-to-selective extinction ratio ( $R_V = 5.0$ , rather than the standard 3.1) that is found to be more appropriate in dense molecular clouds (e.g., Martin & Whittet 1990). The inner radius of the disk structure grid,  $R_{\text{in}}$ , is also set by the stellar properties, based on a crude approximation of where temperatures are high enough to sublimate the dust grains. We define

$$R_{\text{in}} = R_* \left( \frac{T_*}{T_s} \right)^2 = \left( \frac{L_*}{4\pi\sigma T_s^4} \right)^{1/2}, \quad (6)$$

where  $R_*$  is the stellar radius,  $T_s$  is the sublimation temperature and is fixed at 1500 K, and we assume that self-irradiation by the inner disk rim does not substantially contribute to the heating at  $R_{\text{in}}$  (Dullemond et al. 2001). Table 3 lists the relevant stellar parameters and literature references adopted here. Although not explicitly used in the modeling, we include stellar masses and ages in Table 3 that were determined with reference to the Siess et al. (2000) pre-main-sequence stellar evolution models in a Hertzsprung-Russell diagram.

The viewing geometry of the disk, specified by the inclination and position angle on the sky, are required to compute synthetic data from the models. In most cases, we fix the  $\{i, \text{PA}\}$  values based on elliptical Gaussian fits of the continuum visibilities (see §2). Given the sensitivity and angular resolution of our SMA data, these estimates are generally sufficient. For the few cases with clear emission line detections, we can use the resolved CO spatio-kinematics to test and refine those viewing geometry estimates. We first make an estimate of the disk structure using the viewing geometry inferred from the Gaussian fits to the continuum data. That structure model is then used as an input to the non-local thermodynamic equilibrium Monte Carlo radiative transfer code RATRAN (Hogerheijde & van der Tak 2000) to determine CO level populations and compute synthetic visibilities at the same spatial frequencies and velocity channels sampled by the SMA. We assume a Keplerian velocity field based on the stellar masses in Table 3, a turbulent velocity width of  $0.1 \text{ km s}^{-1}$ , and a homogeneous CO abundance of  $\sim 10^{-4}$ - $10^{-5}$  relative to  $\text{H}_2$  (varied to match the line intensities) in regions of the disk where  $T \geq 20 \text{ K}$  (to account for depletion onto dust grains). The synthetic visibilities were compared with the SMA data over a grid of  $\{i, \text{PA}\}$  values to determine a refined viewing geometry estimate (the model fits were then re-performed with the refined  $\{i, \text{PA}\}$  values). In the 3 relevant cases, the initial estimates of  $\{i, \text{PA}\}$  from the Gaussian fits to the continuum data were found to be accurate, lying within  $5^\circ$  for the inclination and  $8^\circ$  for the position angle. As an example, Figure 4 shows the CO channel maps for the AS 209 disk along with the corresponding best-fit model and residuals determined in this way.



### 3.3. Radiative Transfer

For a given set of stellar properties, dust grain population, and density structure as described above, we compute the temperature structure of a model disk and generate synthetic data products with the two-dimensional axisymmetric Monte Carlo radiative transfer code **RADMC** (v3.1), created and developed by C. P. Dullemond. **RADMC** utilizes an algorithm similar to the one described by Bjorkman & Wood (2001) to simulate the propagation of photons through a dust medium that is heated solely by irradiation (in this case from the central star). The basic principles of the **RADMC** code were described by Dullemond & Dominik (2004a). In this version, a diffusion algorithm is employed to calculate temperatures in the densest regions of the disk (near the midplane of the inner disk), where photon statistics are poor in the Monte Carlo simulations. With the results of the radiative transfer calculations, a raytracing program is used to generate a model SED and millimeter continuum visibilities (at the same spatial frequencies  $\{u, v\}$  that were sampled by the SMA observations) for a given viewing geometry. To simulate the smearing effect of atmospheric phase noise, the model visibilities are convolved with a  $0''.1$  Gaussian “seeing” kernel. The small seeing disks inferred here have a minimal impact on the visibilities, but are included for completeness.

### 3.4. Estimating Model Parameters

Our modeling philosophy is based on finding the disk structure parameters that can best reproduce both the de-reddened broadband SED and the SMA continuum visibilities. In practice, this is achieved by varying the 5 free parameters that describe the density structure,  $\{M_d, \gamma, R_c, h_c, \psi\}$ , such that the total  $\chi^2 = \chi_{\text{sed}}^2 + \chi_{\text{vis}}^2$  statistic is minimized (two additional parameters,  $\{R_{\text{cav}}, \delta_{\text{cav}}\}$ , are varied for the SR 21, WSB 60, and DoAr 44 disks). The  $\chi_{\text{vis}}^2$  values are computed as the sum of the  $\chi^2$  values for the real and imaginary components of the visibilities at each individual spatial frequency, with the errors based on the visibility weights and amplitude calibration uncertainty (e.g., Lay et al. 1997; Guilloteau & Dutrey 1998). The broadband SEDs are constructed from the literature (see §4.2 for references in individual cases), and uncertainties at each frequency are computed as the quadrature sum of standard errors and absolute calibration uncertainties. Data shortward of  $0.5 \mu\text{m}$  ( $V$ -band) and near  $10 \mu\text{m}$  are excluded so that the fits are not affected by excess ultraviolet emission from accretion and the detailed shape of silicate emission profiles, respectively. The parameter estimation process begins by computing  $\chi^2$  values over a broad, coarse grid of parameter-space. Those results guide a refined search for a global minimum  $\chi^2$  using the downhill simplex algorithm **AMOEBA** (Press et al. 1992). For the SR 21, WSB 60, and DoAr 44 disks, we explore an abridged parameter-space, with a focus on estimating a size for the central emission cavity ( $R_{\text{cav}}$ ): more detailed modeling will be treated elsewhere (e.g., see Brown et al. 2009).

Because of the finite number of simulated photon packages used in Monte Carlo radiative transfer calculations, the output synthetic data products contain some inherent noise. In general, this noise can be effectively suppressed with a sufficiently large number of photon packages and

the line-of-sight averaging employed in the post-processing raytracing program. However, there is some concern about the Monte Carlo noise manifested in the temperatures near the disk midplane – where the photon statistics are relatively poor in the simulations – because of their direct impact on the synthetic millimeter visibilities (recall  $S_\nu \propto \kappa \Sigma T$ ). To assess the influence of that noise on the local shape of  $\chi^2$ -space used in the AMOEBA minimization algorithm, we performed two “repeatability” tests. First, we conducted RADMC + raytracing calculations multiple times for fixed parameter sets and compared the resulting synthetic data products with the real data and errors. These comparisons indicated that the Monte Carlo noise contributes only minimally to the  $\chi^2$  values, significantly less than the observational uncertainties. And second, we initialized the AMOEBA algorithm with a variety of different parameter sets and compared the end results of the minimization process (i.e., the best-fit parameter values). Those results were not significantly different from one another, again indicating that the Monte Carlo noise does not have an adverse affect on the local shape of  $\chi^2$ -space.

While a simple  $\chi^2$  sum for the independent datasets (visibilities and SED) is the appropriate goodness-of-fit statistic from a purely mathematical viewpoint, it is important to highlight the relative impact of each dataset on the fitting process. For a given disk, there are many more visibilities than SED datapoints ( $N_{\text{vis}}/N_{\text{sed}} > 10^3$ ). However, the signal-to-noise ratios for individual visibilities are substantially lower than for the SED fluxes, such that the relative contribution of each visibility point to the total  $\chi^2$  value is roughly a factor of  $\sim 10^3$  less than that for each individual SED point (within an order of magnitude). In practice, this balance between the quantity and quality of individual datapoints ensures that the total  $\chi^2$  value is appropriately tempered if  $\chi_{\text{sed}}^2$  becomes too large, despite the fact that the large  $\chi_{\text{vis}}^2$  values generally have more influence over the minimization algorithm. This balance is just a fortuitous coincidence, but future interferometric datasets will offer improved sensitivity and vastly increased  $N_{\text{vis}}$ . To continue with this kind of multi-dataset modeling effort with superior millimeter data (e.g., from the *Atacama Large Millimeter Array*), the relative weighting of datasets will need to be re-evaluated. To that end, we experimented with two alternative ways of defining a goodness-of-fit statistic.

In one case, we minimized the sum  $\tilde{\chi}_{\text{vis}}^2 + \tilde{\chi}_{\text{sed}}^2$  of the *reduced*  $\chi^2$  values, defined as  $\tilde{\chi}^2 = \chi^2/\nu$  where  $\nu = N - 5$  is the degrees of freedom in the fit (the number of datapoints less the number of free parameters in the model). However, the relative weightings (i.e., signal-to-noise ratio, SNR) for each dataset imply that  $\tilde{\chi}_{\text{sed}}^2 > \tilde{\chi}_{\text{vis}}^2$  in general, driving the minimization to parameter sets that provide poor matches with the millimeter data. The large  $\tilde{\chi}_{\text{sed}}^2$  values are usually due to relatively small mismatches with the high SNR optical/infrared fluxes, where the detailed stellar properties and heating/scattering near the inner disk rim are important (and not treated in detail here). Therefore, parameter estimation based on this  $\tilde{\chi}^2$  statistic is too much influenced by physical conditions near the star-disk interface that are not of interest here. One could imagine an additional re-weighting scheme as a function of SED wavelength, but it is not clear how to assign those weights nor how such manipulations could affect the best-fit parameter estimates. In a separate experiment, we instead aimed to balance the impact of the two datasets using azimuthally-averaged visibility profiles (see

§4.1 for details) such that  $N_{\text{vis}} \sim N_{\text{sed}}$ . However, the SNR issues persist in this definition and again lead to fits dominated by highly weighted short-wavelength SED points. In the end, we adopt the simple summed  $\chi^2$  statistic initially defined above because it imposes the fewest assumptions upon the data (and still produces quality fits). Similar modeling in the future will likely require some effort to distill the most useful set of information from larger and more sensitive visibility datasets, perhaps akin to some of the clever geometric techniques developed to characterize scattered light images (e.g., Glauser et al. 2008; Pinte et al. 2008).

Although this grid search and AMOEBA minimization technique is able to find a minimum  $\chi^2$  value in the 5-dimensional disk structure parameter-space, it does not provide sufficient information to accurately gauge uncertainties on the best-fit parameter estimates. The computation time required to perform the Monte Carlo radiative transfer calculations outlined above is the limiting factor that makes proper estimates of uncertainties (e.g., from a sufficiently sampled  $\chi^2$  grid search) prohibitive for such a large sample. Since the shape of the surface density profile is of considerable interest, we gauged how accurately we can determine  $\gamma$  by repeating the fitting process described above for various fixed  $\gamma$  values around the best-fit estimate. In general, we find that the fit quality is significantly diminished when these explored  $\gamma$  values deviate from the best-fit value by  $\sim 0.2$ - $0.3$ . A representative example of this process is discussed in §4.1.2. While these are only qualitative estimates of the uncertainties on  $\gamma$ , they are in reasonable agreement with more statistically robust error estimates for similar studies (e.g., Piétu et al. 2007; Isella et al. 2009).

## 4. Results

### 4.1. Disk Structures

The density structure parameter values that best reproduce the data for the six disks with continuous emission distributions are presented in Table 4; those for the remaining three disks with central emission cavities are shown separately in Table 5. Also listed are the fixed values for the inclinations, major axis position angles, and inner disk radii (Table 4 only; see §3.2), as well as the  $\tilde{\chi}^2$  statistics corresponding to the visibility and SED datasets separately (see §3.4). The scale height parameter  $h_c$  has been recast into a more common spatial (rather than angular) format, as described in equation (3). The distributions of the model parameters are shown together in Figure 5. In the following sections, we discuss each of these parameters in the context of the sample as a whole. Commentaries on the results for individual disks are provided in §4.2. The synthetic data produced by the best-fit structure models are compared with the observations in Figures 6 and 7. From left to right in these figures, each row shows the observed millimeter continuum image (as in Figure 1), the best-fit model image synthesized in the same way as the data, the imaged residuals, the broadband SED, and the elliptically-averaged variation of the real part of the visibilities as a function of the deprojected interferometer baseline length.

The “visibility profiles” in the rightmost panels of Figures 6 and 7 conveniently display the

continuum emission at all of the spatial scales that are sampled by the interferometer. The profiles were generated by averaging the visibilities in  $20\text{ k}\lambda$  annular bins in a coordinate system that accounts for the disk viewing geometry. The abscissae mark the deprojected baseline length in this coordinate system,  $\mathcal{R}_{uv} = (d_a^2 + d_b^2)^{1/2}$ , where the major and minor axes are  $d_a = (u^2 + v^2)^{1/2} \sin \phi$  and  $d_b = (u^2 + v^2)^{1/2} \cos \phi \cos i$ , respectively (Lay et al. 1997). Here  $\{u, v\}$  are the Fourier spatial frequency coordinates and  $\phi = \arctan(v/u) - \text{PA}$ . The ordinates show the real part of the visibility flux (averaged in each bin), calculated with an appropriate phase shift to compensate for the centroid position offset relative to the observed phase center. For a circularly symmetric disk that is both vertically and optically thin, the visibility profile constructed in this way represents the Fourier transform of the radial surface brightness distribution. In the Figure 6 and 7 images, crosshairs mark the centroid position and major axis position angle; their relative lengths denote the aspect ratio set by the disk inclination. The model fits are overlaid in red for the SEDs and visibility profiles, and the contributions of the stellar photospheres are shown as blue dashed curves.

Note that we have included higher resolution inset images for the WSB 60 disk in Figure 7. Those images were generated from the same visibility data, but with increased weight on the longer baselines (with  $\text{robust} = -1$  and excluding baselines  $< 40\text{ k}\lambda$ ) to accentuate the continuum structure at small disk radii. The synthesized beam in these insets has dimensions of  $0''.42 \times 0''.22$  at  $\text{PA} = 21^\circ$  ( $\sim 2\times$  higher resolution in the short axis compared to the main image). Despite the symmetric appearance of the WSB 60 disk in the main panel at lower resolution, the inset clearly demonstrates that the emission is not centrally peaked. This behavior was the motivation for using the disk cavity density model in this case. Although some low-level asymmetries are apparent in the data images (e.g., for GSS 39 or AS 209), no significant ( $\geq 3\sigma$ ) deviations from the assumed symmetric models are found in the residual images. As with the model fits, the data–model subtraction is performed on the visibilities, and not in the image plane. Those residual visibilities are then Fourier inverted, deconvolved, and restored with the synthesized beam in the same way as for the data and model (see §2). The absence of significant residual emission associated with these apparent asymmetries implies that their origin is consistent with noise. Comparisons of images made with alternative weightings of the visibility data in the deconvolution process support that conclusion.

In the following sections, we discuss each of the key free parameters in these structure models, their values for the sample as a whole, and their distinct signatures on the observational data. There are three important points to keep in mind: (1) the amount of millimeter continuum emission scales with  $\{M_d, h_c\}$ ; (2) the spatial distribution of that emission is determined by  $\{\gamma, R_c, \psi\}$ ; and (3) in practice, the shape of the infrared SED plays a key role in determining the vertical structure parameters  $\{h_c, \psi\}$ , leaving  $\{M_d, \gamma, R_c\}$  to be constrained by the millimeter data.

#### 4.1.1. Disk Masses ( $M_d$ )

As shown in Figure 5a, the total masses inferred for the sample disks range from  $0.005\text{--}0.14 M_\odot$  (assuming a 100:1 gas-to-dust mass ratio). The disks around SR 21, WSB 60, and DoAr 44 are

associated with the lowest  $M_d$  values (0.005-0.02  $M_\odot$ ), due to the diminished densities in the central regions required to explain the observed emission morphologies. But regardless, the masses for this sample lie at the high end of the combined  $M_d$  distribution for Taurus and Ophiuchus disks (ranging from  $\sim 0.0001$ -0.1  $M_\odot$ ; see Fig. 10 in Andrews & Williams 2007b), highlighting an important sample selection bias. To obtain sufficient sensitivity on long SMA baselines, the sample disks were chosen to be among the brightest 850  $\mu\text{m}$  sources in the Ophiuchus star-forming region. Because of the low optical depths at these wavelengths, bright emission is associated with higher disk masses (Beckwith et al. 1990). Although this sample may not be representative of the median  $\sim 1$  Myr-old disk, the  $M_d$  values inferred here are comparable to or substantially larger than the minimum mass of the primordial solar nebula ( $\sim 0.01 M_\odot$ ; Hayashi 1981). Therefore, the sample includes good examples of the disks that are most capable of making planets, at least in terms of containing a sufficient amount of raw material. However, their true potential for planet formation depends intimately on how that material is distributed spatially.

#### 4.1.2. Surface Density Gradients ( $\gamma$ )

The distribution of mass in the disk is characterized by the parameter  $\gamma$ , which sets the shape of the surface density profile. Figure 5b demonstrates that the disks in this sample have similar  $\Sigma$  profiles, with a narrow range of gradients ( $\gamma \approx 0.4$ -1.0) around the median value,  $\gamma = 0.9$ . That typical value corresponds to a surface density profile that varies roughly inversely with radius in the inner disk ( $\Sigma \propto 1/R$  when  $R \lesssim R_c$ ) and smoothly merges into a steeper exponential decrease at larger radii ( $\Sigma \propto 1/e^R$  when  $R \gtrsim R_c$ ). Figure 8 exhibits the inferred  $\Sigma$  profiles, with the dust surface densities utilized in the modeling scaled up 100 $\times$  to represent the total gas+dust densities. As a reference, the dark gray regions plotted in Figure 8 show the MMSN surface densities for Saturn, Uranus, and Neptune determined by Weidenschilling (1977). The radial widths of those regions mark the annular extent over which the augmented planetary masses were spread, and their heights denote the uncertainties in the chemical composition of the planets relative to cosmic abundances. A more detailed comparison is made in §5.2.

Referring back to the qualitative emission-structure relation,  $S_\nu \propto \kappa \Sigma T$ , we note that  $\gamma$  should have a direct impact on the morphology of the millimeter continuum emission. An examination of Figure 8 demonstrates that the inner disk – where  $\Sigma \propto 1/R^\gamma$  – is generally not well-resolved, even with the maximal resolution scale afforded by the SMA data (marked in light gray). Therefore, the observed emission morphologies are most sensitive to the shape (and location) of the  $\Sigma$  taper in the outer disk, where  $\Sigma \propto 1/\exp(R^{2-\gamma})$ . Such behavior implies that smaller  $\gamma$  values produce more centrally-concentrated emission morphologies, or steeper surface brightness profiles. It is worthwhile to point out that this is exactly the opposite relationship between the emission distribution and the gradient  $p$  in the standard power-law assumption for surface densities, where  $\Sigma \propto R^{-p}$  out to some cut-off radius (e.g., Andrews & Williams 2007a).

This relation between  $\gamma$  and the emission morphology is manifest in Figure 9, which serves as

a qualitative demonstration of how accurately we can measure  $\gamma$  values (see §3.4 for details). In this figure, we show the SED and visibility profile data for the WaOph 6 disk (as in Figure 6) with the best-fit  $\gamma = 1.0$  models overlaid in red. The blue and green curves show the models that best reproduce the data for  $\gamma$  values fixed at 0.8 and 1.2, respectively. All three of these models match the SED well, but there are clear differences between them in a comparison with the observed visibilities. Because the data probe a steeper  $\Sigma$  taper for the  $\gamma = 0.8$  (blue) model compared to  $\gamma = 1.0$  (red), we observe a steeper brightness profile with more emission concentrated on smaller spatial scales. In terms of the visibility profiles, this results in the  $\gamma = 0.8$  model over-predicting the amount of emission on the longest baselines. The exact opposite is true for the  $\gamma = 1.2$  (green) model. We should emphasize that while Figure 9 demonstrates the connection between  $\gamma$  and the observations, it is only representative of a qualitative exploration of parameter space, and not a formal statistical characterization of the uncertainties on  $\gamma$ .

#### 4.1.3. Characteristic Radii ( $R_c$ )

Figure 5c shows that the characteristic radii that govern where the  $\Sigma$  profiles transition from power-laws to exponential tapers lie in the range  $\sim 20$ -200 AU for the sample disks. A larger  $R_c$  generally means more emission on larger spatial scales, although the role of this parameter as a fulcrum in the  $\Sigma$  and  $h$  radial profiles can complicate that behavior. Since these characteristic radii will play a key role in a discussion of viscous evolution models (§5.1), it is worth reiterating that they are not the same as the standard cut-off radius ( $R_c \neq R_{\text{out}}$ ). As mentioned in §3.1, sharp outer edges are disfavored by resolved optical observations (McCaughrean & O’Dell 1996) and a comparison between millimeter continuum and CO spectral images (Hughes et al. 2008). Moreover, the new continuum data presented here show no evidence for the visibility nulls that would be produced by such sharp edges (with the notable exceptions of the disks around SR 21, WSB 60, and DoAr 44).

#### 4.1.4. Vertical Structure ( $h_c$ and $\psi$ )

Recall that the millimeter continuum emission from a disk scales with the product of density and temperature ( $S_\nu \propto \kappa \Sigma T$ ). In our models, the temperature structure is determined by how effectively the disk material intercepts and reprocesses energy from the star. Most of that energy is absorbed by dust grains at some height above the disk midplane, creating an intimate connection between the vertical structure of the disk and its temperature distribution. In a flared disk, a large surface area of dust can be directly irradiated by the star. Therefore, more energy will be absorbed in the disk atmosphere and subsequently re-emitted, both into space and deeper into the disk interior. In essence, vertically extended (larger  $h_c$ ) disks are heated more efficiently, emit more from their atmospheres, and have higher interior temperatures. Consequently, a larger  $h_c$  produces brighter emission at both infrared and millimeter wavelengths. By controlling the vertical extent

of the disk at different radii, the scale-height gradient  $\psi$  determines how stellar energy is deposited into the disk atmosphere as a function of radius. Steeply flaring disks (larger  $\psi$ ) will re-emit more of that energy from larger radii, both outward toward an observer and inward to heat the disk interior. Since cooler dust preferentially emits at longer wavelengths, a larger  $\psi$  will generate a flatter infrared SED. Likewise, a larger  $\psi$  results in a flatter temperature profile in the disk interior, and therefore a more diffuse millimeter emission morphology (a flatter surface brightness profile).

The histograms in Figure 5d,e show scale heights from 4-20 AU (at a fiducial radius of 100 AU) and  $\psi$  values from 0.04-0.26 for the sample disks. While these numerical ranges are small, they represent a diverse set of vertical structures – from flat and cold (e.g., WaOph 6) to flared and warm (e.g., AS 205). Figure 10 shows the radial temperature profiles at the disk midplanes, derived from the radiative transfer calculations (§3.3; for clarity, the disks with central cavities are not shown). These profiles generally behave as power-laws,  $T \propto R^{-q}$  with  $q \approx 0.5-0.6$  over a wide range of radii, from just beyond  $R_{\text{in}}$  out to  $\sim R_{\text{c}}$ . At larger radii, the exponential  $\Sigma$  taper facilitates a more efficient heating of the disk interior, resulting in a flatter midplane  $T$  profile ( $q \approx 0.3-0.4$ ). The disks with surface density discontinuities (around SR 21, WSB 60, and DoAr 44) have  $T$  profiles with a distinct kink and hotter temperatures around  $R_{\text{cav}}$ , marking the rarefied dust regions just interior to where the higher density outer disk is frontally illuminated by the star.

#### 4.1.5. Central Cavity Properties ( $R_{\text{cav}}$ and $\delta_{\text{cav}}$ )

To reproduce the diminished millimeter emission in the central regions of the disks around SR 21, WSB 60, and DoAr 44, we introduced two additional parameters  $\{R_{\text{cav}}, \delta_{\text{cav}}\}$  that act to decrease the surface densities inside a disk cavity. The scaled-down densities of warm dust inside the cavity reduce the amount of infrared excess emission, producing a deficit in the SED compared to a disk with a continuous density distribution. The location of the cavity edge,  $R_{\text{cav}}$ , determines the wavelength where the SED deficit recovers; larger  $R_{\text{cav}}$  values produce SED deficits out to longer infrared wavelengths (corresponding to cooler temperatures). The depth of the SED deficit is set by the parameter that scales down the densities,  $\delta_{\text{cav}}$ ; a smaller value (an emptier cavity) generates less emission and therefore a deeper deficit. The diminished  $\Sigma$  values also lead to a proportional decrease in the millimeter emission inside the cavity, producing a ring-like morphology (see Fig. 7). The sharp density change at the cavity edge generates a null in the millimeter visibilities at a spatial frequency associated with the edge location,  $R_{\text{cav}}$  (Hughes et al. 2007); larger  $R_{\text{cav}}$  values produce nulls at shorter baselines. The density contrast in the cavity sets the emission levels on small spatial scales, such that a lower  $\delta_{\text{cav}}$  produces a more pronounced null.

In practice, our modeling relies heavily on the location and depth of that null to determine the values of  $\{R_{\text{cav}}, \delta_{\text{cav}}\}$ , due to the relatively sparse infrared SED coverage for these disks. Those parameters are expected to be degenerate with the structure parameters of the remnant outer disk because of the short spatial dynamic range available in that region. Moreover, the cavity parameters derived here are only appropriate for the simple model assumptions that were made in §3.1. Their

values would be modified depending on the details of the cavity edge (e.g., an irradiated “wall”; D’Alessio et al. 2005; Hughes et al. 2009) or the dust content in the cavity interior. For example, others have typically adopted smaller dust grain sizes ( $a_{\max} \sim 1\text{-}10 \mu\text{m}$ ) inside disk cavities to more faithfully reproduce infrared spectra (e.g., Calvet et al. 2005) and accommodate calculations that track inward dust filtration from the outer disk (Rice et al. 2006). Compared to the grain size distribution adopted here, those smaller grains have opacities that are lower at millimeter wavelengths and higher in the infrared. Even meager densities of such small dust grains inside the cavity can produce substantial infrared emission without changing the millimeter continuum. Perhaps this is a solution that would better reproduce the observations for a case like the DoAr 44 disk. Alternatively, a “gap” model, where the cavity contains a detached remnant of the inner disk, could generate similar observational signatures (e.g., Espaillat et al. 2007, 2008).

#### 4.1.6. *Comments on Parameter Degeneracies*

In practice, the different structure parameters used here can have similar effects on the data, leading to some basic model degeneracies. For example,  $M_d$  and  $h_c$  have the same scaling effect on the amplitude of millimeter emission, while  $\gamma$  and  $\psi$  have similar impacts on how that emission is distributed spatially. Fortunately, those degeneracies are alleviated by requiring the models to fit the SED and millimeter visibilities jointly. For instance, unlike the surface density parameters  $\{M_d, \gamma\}$ , the scale height parameters  $\{h_c, \psi\}$  can be constrained through their strong impact on the infrared SED. However, some model degeneracies remain, perhaps most notably between  $\gamma$  and  $R_c$ . Mundy et al. (1996) first discussed an analogous degeneracy between emission gradients and size scales, demonstrating that the data can sometimes be explained equally well by trading off steeper gradients and larger sizes (see also Andrews & Williams 2007a). In our models, this degeneracy is slightly complicated due to the form of the  $\Sigma$  profile adopted in §3.1. For low  $\gamma$  values, the surface density (and therefore emission) profile is similar to a power-law + cutoff model; therefore, the data can accommodate larger  $\gamma$  values by increasing  $R_c$ . However, as  $\gamma$  gets larger the data are increasingly insensitive to  $R_c$ , and its precise value becomes difficult to determine. The experiments to estimate how well  $\gamma$  can be constrained (see §3.4 and §4.1.2) indicate that this degeneracy is quantitatively weaker than in previous studies, due to the improved spatial dynamic range of the data.

#### 4.1.7. *Comments on Opacities*

All estimates of disk structure parameters are degenerate with the assumed opacities. There are two distinct structure-opacity relationships that merit attention. First, and perhaps most straightforward, is a density-opacity degeneracy related to interpreting the millimeter continuum emission. Because that emission is optically thin, it is sensitive to the optical depth, the product  $\kappa\Sigma$ . For a given brightness, lower opacities would lead us to infer higher densities, and vice versa.



Likewise, spatial opacity variations would affect constraints on the shape of the  $\Sigma$  profile ( $\gamma$ ). For example, a radial opacity gradient might be a natural outcome of the grain growth process (e.g., Dullemond & Dominik 2005; Garaud 2007). Higher densities and velocities in the inner disk would decrease growth timescales compared to larger radii, leading to an opacity profile that increases with radius. By assuming a spatially uniform  $\kappa$ , we could underestimate  $\gamma$  in the inner disk. Disentangling this density-opacity ambiguity is a formidable challenge, but some progress is feasible by exploiting the shape of the millimeter continuum spectrum (e.g., Beckwith & Sargent 1991; Rodmann et al. 2006). In the future, spatially resolved millimeter SEDs could help characterize the relative grain growth efficiencies at different locations throughout the disk.

A second degeneracy between the vertical structure of the disk and the opacity is more difficult to quantify in a generic way. The energy from stellar radiation is deposited in the disk atmosphere, at a location that depends on the optical/infrared opacities. If those opacities are low, stellar radiation can penetrate deeper into the disk before it is absorbed and then re-processed, and vice versa. Therefore, a given SED can be reproduced by various combinations of vertical structures and material opacities. In our models, we have fixed the opacities and varied some vertical structure parameters to reproduce the SEDs. Some studies have taken a different approach, effectively fixing the vertical structure (to be in hydrostatic equilibrium) and varying the opacities as a function of height in the disk (e.g., D’Alessio et al. 2006). In either case, the opacities are tied to the vertical structure, and therefore the disk temperature structure (§4.1.4). Because the millimeter continuum emission depends on  $\kappa\Sigma T$ , the uncertain opacities in the disk atmosphere can indirectly impact our constraints on  $\Sigma$ . This degeneracy can potentially be alleviated using independent constraints on the vertical structure of the disk, either with multi-transition molecular line data (e.g., Dartois et al. 2003) or high resolution scattered light images (e.g., Pinte et al. 2008).

## 4.2. Commentary on Individual Disks

**AS 205** – Located in the northern outskirts of the main Oph clouds, AS 205 is a hierarchical triple system: the K5 primary (AS 205 A) lies  $1''.3$  northeast of a K7/M0 spectroscopic binary (AS 205 B; Ghez et al. 1993; Prato et al. 2003; Eisner et al. 2005). Roughly 95% of the  $860\ \mu\text{m}$  emission from the system originates in a disk around the primary, which is the focus in this paper. The remainder (50-60 mJy) is associated with the AS 205 B binary (see Fig. 1). Bright CO  $J=3-2$  emission ( $\sim 65\ \text{Jy km s}^{-1}$ ) centered on the primary star shows a small velocity gradient along the disk major axis, indicative of a low inclination ( $i = 25^\circ$ ) viewing geometry (Fig. 2). However, spatio-kinematic asymmetries in the direction of the secondary are present in the CO channel maps, suggesting that some of the line emission is associated with AS 205 B. Previous interferometric observations were unable to resolve the emission from the AS 205 A/B components (Andrews & Williams 2007a).

We constructed a SED for AS 205 A using component-resolved photometry from  $\sim 0.5\text{-}12\ \mu\text{m}$  (Cohen & Kuhl 1979; Liu et al. 1996; McCabe et al. 2006). Composite 25 and  $60\ \mu\text{m}$  flux densities (Weaver & Jones 1992) were split based on a simple extrapolation of the resolved A and B pho-

tometry and ground-based spectra (Schegerer et al. 2006) at shorter wavelengths. Millimeter flux densities were determined by partitioning single-dish photometry (350, 450, and 1300  $\mu\text{m}$ ; Andrews & Williams 2007a,b) according to the resolved 860  $\mu\text{m}$  A/B flux ratio found here. The resulting infrared SED is the brightest in the sample relative to the stellar photosphere, driving the model fits to infer a particularly extended vertical structure. But given the complications associated with the small angular separation between the A and B components, a combined structure analysis of both disks would be beneficial in the future.

**GSS 39** – This heavily reddened M0 star in the L1688 dark cloud hosts a bright, well-resolved millimeter continuum disk (Fig. 1). Resolved CO  $J=3-2$  emission is found centered on GSS 39, with a velocity gradient oriented along the major axis of the continuum disk. However, there is substantial contamination from cloud material that prohibits a more detailed analysis. The high extinction ( $A_V \approx 15$ ) produced by that cloud material forces us to base our stellar luminosity estimate on photometry in the near-infrared (2MASS; Cutri et al. 2003), rather than at optical wavelengths. Given the non-negligible disk emission at  $\lambda \geq 1 \mu\text{m}$ , there is considerable uncertainty on  $L_*$  that propagates to the disk structure parameter estimates. The remainder of the SED was collected from the *Spitzer* c2d Legacy project (Evans et al. 2003), ground-based infrared photometry (Lada & Wilking 1984), and 350-1200  $\mu\text{m}$  single-dish flux densities (Stanke et al. 2006; Andrews & Williams 2007b). The GSS 39 disk is the only case our study has in common with the recent 1.3 mm interferometric survey by Isella et al. (2009). Despite using different modeling procedures, we find similar disk parameters within the quoted uncertainties.

**AS 209** – This young K5 star, relatively isolated from the main Ophiuchus clouds, was found to harbor a Keplerian molecular gas disk by Koerner & Sargent (1995). That structure is confirmed here (Figs. 2 and 4), where the spatially resolved CO  $J=3-2$  line emission ( $\sim 16.5 \text{ Jy km s}^{-1}$ ) has a clear rotation signature consistent with a disk inclined  $\sim 40^\circ$  from face-on. While broadband SED information for AS 209 is sparse, we adopt averaged optical data from variability studies (Herbst et al. 1994; Grankin et al. 2007), ground-based and *IRAS* infrared photometry (Hamann & Persson 1992; Weaver & Jones 1992; Cutri et al. 2003), and single-dish millimeter flux densities (André & Montmerle 1994; Andrews & Williams 2007b). A publicly available  $\sim 5-30 \mu\text{m}$  *Spitzer* IRS spectrum from the c2d Legacy project (Evans et al. 2003) is dominated by broad silicate emission features, and therefore not used in our modeling. The absence of useable  $\sim 5-60 \mu\text{m}$  SED data means that the inferred vertical structure is particularly uncertain in this case. Moreover, it implies that the millimeter visibilities play a comparatively larger role in the parameter estimates. Perhaps the lack of infrared SED data contributes to the AS 209 disk having the lowest  $\gamma$  value (0.4) in the sample.

**DoAr 25** – A K5 star in the L1688 dark cloud, DoAr 25 hosts a resolved optical/infrared scattered light disk (K. R. Stapelfeldt 2008, private communication) that is also particularly bright at millimeter wavelengths. Despite these substantial disk signatures, the standard hallmarks of

accretion for the DoAr 25 disk are comparatively meager: estimates of the mass accretion rate range from low ( $3 \times 10^{-9} M_{\odot} \text{ yr}^{-1}$ ; Greene & Lada 1996; Luhman & Rieke 1999) to negligible ( $< 2 \times 10^{-10} M_{\odot} \text{ yr}^{-1}$ ; Natta et al. 2006) values. The SED also shows a relatively small excess over the stellar photosphere from  $\sim 1\text{--}15 \mu\text{m}$  (Fig. 6) compared to typical T Tauri disks, although a more substantial excess is present at longer wavelengths. We constructed the DoAr 25 SED from optical data (Vrba et al. 1993; Wilking et al. 2005), the 2MASS database (Cutri et al. 2003), *Spitzer* observations (Evans et al. 2003; Padgett et al. 2008), and single-dish millimeter photometry (André & Montmerle 1994; Dent et al. 1998; Andrews & Williams 2007b).

In an effort to model these same SMA data while accounting for the small infrared excess and low accretion rate, Andrews et al. (2008) suggested that the DoAr 25 disk has a shallow density distribution,  $\Sigma \propto R^{-0.34}$ . We find a steeper inner disk  $\Sigma$  profile in our fits ( $\Sigma \propto R^{-0.9}$  when  $R \lesssim 80 \text{ AU}$ ), which utilize different assumptions for some key aspects of the modeling process: (1) a smaller distance (125 pc, compared to 145 pc) shortens spatial scales and makes radial profiles steeper; (2) a smaller  $L_*$  ( $0.8 L_{\odot}$ , compared to  $1.3 L_{\odot}$ ) decreases disk temperatures and leads us to infer different vertical structure parameters; and (3) a more appropriate treatment of the visibilities in the fitting process (i.e., using each visibility point, rather than the binned visibility profile) places less emphasis on a detailed match to the infrared SED (see §3.4). Because of these differences, we find a best-fit model with a larger flaring angle ( $\psi = 0.15$ , compared to 0.11), leading to a flatter midplane  $T$  profile that requires a comparatively steeper  $\Sigma$  profile to reproduce the observed visibilities (see §4.1.4). While we find a lower  $\chi^2$  value than for the Andrews et al. (2008) results, we note that  $\Sigma$  profiles with gradients as low as  $\gamma \approx 0.5$  are also able to reproduce the data fairly well. A more robust conclusion could be made in a future modeling study that incorporates the scattered light morphology and a more detailed infrared spectrum to help independently constrain the vertical structure of the disk.

**WaOph 6** – This K6 star is located north of the main Oph clouds, close to AS 209. In addition to a compact millimeter continuum emission morphology, the WaOph 6 disk exhibits CO  $J=3\text{--}2$  line emission ( $\sim 13.5 \text{ Jy km s}^{-1}$ ) with a clear velocity gradient along the disk major axis. While the spatio-kinematics of that CO emission in the channel maps is consistent with a Keplerian rotation pattern inclined  $\sim 40^\circ$  from face-on, there is some cloud contamination near the systemic velocity. The SED used here is composed of the optical/infrared measurements by Eisner et al. (2005), *Spitzer* data from Padgett et al. (2006), and single-dish millimeter photometry (André & Montmerle 1994; Andrews & Williams 2007b). The infrared SED has a steep spectral slope (Fig. 6), consistent with a flat disk geometry where dust grains have largely settled toward the disk midplane. This vertical structure results in a steep midplane temperature profile (Fig. 10), with a particularly cold outer disk. Despite the large  $R_c$  value inferred for the WaOph 6 disk, those low temperatures at large radii lead to the observed compact emission morphology.

**VSSG 1** – The disk around this heavily extinguished M0 star in the L1688 cloud has the most compact, centrally concentrated millimeter emission in the sample. Bright CO  $J=3-2$  emission with significant cloud contamination is found around the star in two distinct LSR velocity intervals centered at  $-3.0$  and  $-0.4 \text{ km s}^{-1}$ . It is unclear if any of that emission is associated with the disk. As with the GSS 39 disk, high extinctions force us to estimate an uncertain  $L_*$  in the near-infrared (Cutri et al. 2003). The ambiguity in that luminosity estimate translates directly to our estimates of disk structure parameters. The remainder of the SED was compiled from the c2d *Spitzer* database (Evans et al. 2003) and single-dish millimeter photometry data (Stanke et al. 2006; Andrews & Williams 2007b). The infrared SED is similar to WaOph 6, with a steep spectral gradient indicative of a relatively flat geometry. Given the compact continuum emission, it is not surprising that we find a small radius ( $R_c = 33 \text{ AU}$ ).

**SR 21** – A large central cavity in the disk around this G3 star was first inferred from the broadband SED (Brown et al. 2007), and then confirmed with the archival (V configuration) SMA data presented here (Pontoppidan et al. 2008; Brown et al. 2009). The SED shown in Figure 7 was compiled from optical (Chini et al. 1981; Vrba et al. 1993) and near-infrared photometry (Cutri et al. 2003), the *Spitzer* c2d Legacy database (Evans et al. 2003), older *IRAS* measurements (Weaver & Jones 1992), and millimeter photometry from  $350 \mu\text{m}$  to  $2.7 \text{ mm}$  (André & Montmerle 1994; Andrews & Williams 2007b; Patience et al. 2008). Our new lower resolution (S configuration) SMA observations do not show any clear evidence for CO  $J=3-2$  emission from the SR 21 disk, although cloud contamination may obscure a weak signal. On the contrary, Pontoppidan et al. (2008) find infrared emission lines from molecular gas inside the SR 21 disk cavity. With a simplistic model, we place the inner edge of that cavity at  $R_{\text{cav}} \approx 37 \text{ AU}$ , further than the  $18 \text{ AU}$  inferred by Brown et al. (2007) from the SED alone. But considering the major differences in model assumptions (particularly the stellar properties), the discrepancy is likely not significant. A more in-depth modeling analysis of the SED and resolved continuum data together will be performed elsewhere (Brown et al. 2009), and should provide more robust constraints on the cavity dimensions.

**WSB 60** – With a spectral type of M4, this cool star in the L1688 cloud is significantly less massive than the rest of the sample. Nevertheless, it harbors one of the brightest millimeter disks in the Oph star-forming region, with a remarkable low-density cavity noted on scales near the SMA angular resolution limit ( $R_{\text{cav}} \approx 20 \text{ AU}$ ). The SED used here was compiled from the optical survey by Wilking et al. (2005), the 2MASS database (Cutri et al. 2003), *Spitzer* photometry (Evans et al. 2003; Padgett et al. 2008), and integrated millimeter flux densities ( $350\text{-}1300 \mu\text{m}$ ; Andrews & Williams 2007a,b). The cavity imaged in the inset of Fig. 7 can be confirmed with a close examination of the visibility profile, which shows that the real part of the visibility fluxes lie below zero on deprojected baselines longer than  $\sim 350 \text{ k}\lambda$ . With such a low stellar mass and a large central cavity, this source certainly merits a follow-up modeling study with a more complete SED dataset.

**DoAr 44** – This young K3 star in the L1688 cloud appears to be a typical classical T Tauri star, and was selected for this survey only because of its brighter than average millimeter emission. The broadband SED is typical of a normal continuous disk, constructed here from optical data (Herbst et al. 1994), the 2MASS database (Cutri et al. 2003), ground-based images (Greene et al. 1994), *Spitzer* photometry (Evans et al. 2003; Padgett et al. 2008), and single-dish millimeter flux densities (Nürnberg et al. 1998; Andrews & Williams 2007b). Nevertheless, the observed double-peaked morphology of the millimeter emission for the DoAr 44 disk (Fig. 1) is a clear signature of an inclined ring, with a lack of emission in the inner disk. Although we make a preliminary estimate for the inner edge of that disk cavity at  $R_{\text{cav}} \approx 33$  AU, there is substantial uncertainty due to the poor fit of the infrared SED. A relatively bright  $\text{H}\alpha$  line ( $42\text{\AA}$ ; Guenther et al. 2007) and substantial infrared excesses confirm that there is a substantial amount of material inside this millimeter emission cavity. A more sophisticated effort to model the inner region of the DoAr 44 disk using the SED, SMA visibilities, and the *Spitzer* IRS spectrum will be presented elsewhere.

## 5. Discussion

### 5.1. Viscous Disk Evolution

For most of its lifetime, the structural evolution of a disk will be determined by the viscous and gravitational interactions that govern the accretion process. The Keplerian rotation and anomalous turbulent viscosities of the disk material combine to drive a net mass flow inwards to smaller radii (Lynden-Bell & Pringle 1974), where magnetic fields can channel it onto the stellar surface (e.g., Königl 1991; Shu et al. 1994). Meanwhile, to balance the angular momentum lost in that process, some disk material is transported out to larger radii (e.g., Pringle 1981). These coupled effects act to decrease densities at smaller radii as the disk expands: the disk structure literally spreads itself thin over time. Empirical constraints on this viscous mode of disk structure evolution are critical for developing improved models of planet formation and various disk dissipation mechanisms.

For the case where disk viscosities are static (constant with time) and spatially distributed like a power-law,  $\nu \propto R^\gamma$ , Lynden-Bell & Pringle (1974) derived an analytic similarity solution for the viscous evolution of the disk surface density profile. The form of that similarity solution (see Hartmann et al. 1998, and the Appendix) is identical to the one adopted in equation (4) when

$$R_c = R_1 \mathcal{T}^{1/(2-\gamma)} \quad (7)$$

$$M_d = M_{d,0} \mathcal{T}^{-1/2(2-\gamma)}, \quad (8)$$

where  $R_1$  is a scaling radius,  $\mathcal{T}$  is a dimensionless time parameter, and  $M_{d,0}$  is the initial disk mass. The time parameter  $\mathcal{T} = 1 + t/t_s$ , where  $t$  is the time since viscous evolution began and  $t_s$  is the viscous timescale. In essence,  $\mathcal{T}$  tracks how many viscous timescales have elapsed. In its initial configuration ( $t = 0$ ;  $\mathcal{T} = 1$ ),  $\sim 60\%$  of the disk mass was concentrated inside the radius  $R_1$ .

Hartmann et al. (1998) explored the prominent role that the surface density/viscosity gradi-

ent ( $\gamma$ ) plays in the evolution of observable disk structure parameters. For a given set of initial conditions, they showed that a larger  $\gamma$  value leads to accelerated viscous spreading (expansion to conserve angular momentum). That relationship is encapsulated in equation (7), where the characteristic radius ( $R_c$ ) determined in our model fits is an empirical measure of how much the disk has expanded since its initial configuration ( $R_c = R_1$  when  $\mathcal{T} = 1$ ). For the typical value  $\gamma = 0.9$  found in this sample,  $R_c$  increases roughly linearly with  $\mathcal{T}$ . Because it is not clear when the evolutionary clock for a given disk was started ( $\mathcal{T}$  is unknown), a precise calibration of the initial conditions  $\{R_1, M_{d,0}\}$  for these viscous models is a challenge. Associating  $\mathcal{T}$  with stellar ages can be problematic, as this simple viscous evolution behavior may not have been applicable for a significant fraction of that time. Figure 11 illustrates how these initial conditions depend on the unknown value of  $\mathcal{T}$ , based on the current disk structures derived in §4 (see equations [7-8]). Note that these plots do not track the evolution of  $\{R_1, M_{d,0}\}$ : the initial conditions *do not change with time*. Rather, they mark what their appropriate values would be for a given value of  $\mathcal{T}$ . For example, if 10 viscous timescales have elapsed since the WaOph 6 disk began its evolution ( $\mathcal{T} = 11$ ), then the current disk structures imply that the initial disk mass was  $M_{d,0} \approx 0.27 M_\odot$ , and 60% of that mass ( $0.16 M_\odot$ ) was initially contained inside  $R_1 \approx 12$  AU. Similar examples for each disk can be made from the initial conditions in Table 6, where we have listed what the  $\{R_1, M_{d,0}\}$  values would be if 1 or 10 viscous timescales have elapsed ( $\mathcal{T} = 2$  and 11).

Aside from providing some limited insight on the initial conditions, our estimates of  $\{\gamma, R_c\}$  help characterize another key radius

$$R_t = R_c \left[ \frac{1}{2(2 - \gamma)} \right]^{1/(2-\gamma)} \quad (9)$$

that marks where the mass flow through the disk changes direction (to conserve angular momentum); material moves in toward the central star for  $R < R_t$  and out to larger disk radii for  $R > R_t$ . In this sample, we find  $R_t$  values of  $\sim 10$ -100 AU (see Table 6; note that  $R_t = R_c/2$  when  $\gamma = 1$ ). Aside from these constraints on  $R_t$ , the only observational diagnostics of the mass flow in disks are the stellar accretion rates,  $\dot{M}_*$ . Hartmann et al. (1998) demonstrated that those accretion rates would decay more rapidly with  $\mathcal{T}$  for larger  $\gamma$  values. They used a power-law fit to the empirical  $\dot{M}_*$ -age relation for T Tauri disks to infer that  $\gamma = 1$  (or larger), in excellent agreement with the results from our parametric structure fits (see also Calvet et al. 2000).

Only a few observational studies have attempted to constrain disk surface densities in the context of these viscous evolution models. Kitamura et al. (2002) fitted the SEDs and 2 mm images ( $\sim 1''$  resolution) for 13 disks with a 1-D structure model. They found a range of  $\gamma$  values from 0.0-0.8, and comparable  $R_c$  values that appeared to be anticorrelated with the  $H\alpha$  line luminosities. Hughes et al. (2008) used a simple (vertically isothermal) 2-D structure model to reproduce both the continuum and CO line visibilities ( $\sim 1$ -2'' resolution) for 4 disks with  $\gamma = 0.7$ -1.1. And most recently, Isella et al. (2009) fitted the 1.3 mm visibilities ( $\sim 0''.7$  resolution) for 14 disks with a “two-layer” structure model (cf., Chiang & Goldreich 1997). Their results suggested a wide range of  $\gamma$  values, from  $-0.5$  to 0.8, and characteristic radii similar to those presented here. Isella et al.

(2009) also argue that their  $R_t$  values are correlated with stellar age. Spatial resolution mismatches, distinct modeling styles, and deviating opacity prescriptions all play some role in explaining the differences in the  $\gamma$  values inferred here (and by Hughes et al.) and those at the low end of the ranges found by Kitamura et al. (2002) and Isella et al. (2009). We do not find any convincing evidence for correlations between the disk structures and stellar properties or accretion diagnostics, but this may be the result of limitations in the sample size and properties.

Various theoretical perspectives have argued for  $\gamma$  values similar to those found with our parametric structure modeling. Hartmann et al. (1998) pointed out that  $\gamma \approx 1$  would be expected for an irradiated disk in vertical hydrostatic equilibrium if the turbulent viscosity parameter,  $\alpha$ , is roughly constant with radius (see below). In a new approach that treats the viscous evolution of magnetized disk material, Shu et al. (2007) predicted steep surface density profiles with  $\Sigma \propto R^{-3/4}$ . A sequence of sophisticated numerical modeling studies that self-consistently track both the formation and subsequent evolution of disks have suggested that larger values near  $\gamma \approx 1.5$  are more appropriate (Vorobyov & Basu 2007; Vorobyov 2008, but see Hueso & Guillot 2005). The  $\Sigma$  profiles in those models correspond to gravitationally unstable, non-axisymmetric disk structures with significantly more mass than has been estimated from observations. However, Vorobyov & Basu (2009) demonstrate that those instabilities and azimuthal asymmetries would quickly damp out when turbulent viscosities are included in the simulations, producing  $\Sigma$  profiles ( $\gamma \approx 0.8$ ), disk masses, and accretion rates that are more in line with those estimated here and elsewhere.

While observational constraints on surface density profiles help characterize how material is redistributed over time within these disks, the pace of that evolution is set by the disk viscosities. The physical origin of those viscosities remains uncertain, although various mechanisms that could drive large-scale turbulent motions in these disks have been suggested as possibilities. Shakura & Sunyaev (1973) proposed a simple prescription for turbulent viscosities,  $\nu = \alpha c_s H$ , where  $c_s$  is the sound speed,  $H$  is the scale height, and  $\alpha$  is a key parameter that characterizes the efficiency of angular momentum transport. Incorporating that relation into our formulation for the structure of viscous disks, we can solve for the viscosity parameter

$$\alpha \approx \frac{\dot{M}_*}{3\pi\Sigma_c} \left( \frac{R}{R_c} \right)^\gamma \frac{1}{c_s H} \quad (10)$$

where  $\Sigma_c$  is defined in equation (5) (see the Appendix). For the disk structures and accretion rates in this sample, we find the wide distribution of  $\alpha$  values shown in Figure 12 and listed in Table 6, ranging from 0.0005 to 0.08. These calculations use the  $\dot{M}_*$  values in Table 6, which were derived directly from emission line fluxes (or  $U$ -band excesses) in the literature using the standard data–accretion luminosity conversions (Muzerolle et al. 1998; Calvet et al. 2004) to force consistency with our adopted stellar properties. The histogram in Figure 12 technically corresponds to  $\alpha$  measured at  $R = 10$  AU, but we show in the Appendix that these values have only a weak radial dependence. The  $\alpha$  values inferred from the disk structures are in good agreement with those found in numerical magnetohydrodynamics simulations, where the magnetorotational instability (Balbus & Hawley 1991) is the mechanism responsible for generating the anomalous turbulent viscosities

(e.g., Hawley et al. 1995; Stone et al. 1996; Fleming & Stone 2003; Fromang et al. 2007).

## 5.2. Planet Formation Potential

Although the surface density profiles for this sample are in good agreement with viscous disk models, they are different than the common prescription for the primordial solar disk (the MMSN). As with the model fits in §4, there are considerable uncertainties in constructing a  $\Sigma$  profile for the MMSN: the abundances of key elements in current planet compositions, the arbitrary assignment of annular bins to smear out augmented masses, and the implicit assumption that the nebular material was stationary throughout its evolution, to name a few (see Cameron 1988; Desch 2007; Crida 2009). But if the zones around Mercury and Mars are ignored due to the high likelihood of their dynamical depletion, the *in situ* augmented planetary densities can be fit reasonably well with a  $\Sigma \propto R^{-1.5}$  profile (Weidenschilling 1977; Hayashi 1981). A steeper  $\Sigma \propto R^{-2.2}$  profile has been argued for by Desch (2007), who uses modified planetary accretion zones motivated by dynamical simulations of the early solar system. A similar  $\Sigma \propto R^{-2}$  profile was determined from the combined properties of 12 extrasolar multi-planet systems (Kuchner 2004). As an alternative, Davis (2005) has suggested a viscous disk model with a flatter inner disk  $\Sigma$  profile corresponding to  $\gamma \approx 0.5$ .

A direct comparison of the density structures for the sample disks and the MMSN was shown in Figure 8. Alternatively, Figure 13 compares how the encircled mass varies with radius in the disks and MMSN. The latter is defined as the cumulative mass interior to a given radius,  $M(<R) = \int \Sigma 2\pi R dR$  from  $R_{\text{in}}$  to  $R$ . Unlike the  $\Sigma$  profile, the MMSN encircled masses do not rely on the arbitrary widths and locations of annular bins. The error bars reflect the uncertainties in the augmented  $M(<R)$  values for Saturn, Uranus, and Neptune in the MMSN and those planets interior to them (particularly Jupiter; Weidenschilling 1977). The dark gray region shows the encircled masses implied by the standard  $\Sigma \propto R^{-1.5}$  MMSN profiles of Hayashi (1981, *lower bound*) and Weidenschilling (1977, *higher bound*). Despite their flatter  $\Sigma$  profiles, Figures 8 and 13 illustrate that the mass distributions for the sample disks are comparable to the MMSN values, within the uncertainties. Particularly good agreement is noted in the resolved Uranus-Neptune region (with the exception of the AS 209 disk). The sample disks have  $\Sigma = 30\text{-}100 \text{ g cm}^{-2}$  at 19 AU,  $15\text{-}60 \text{ g cm}^{-2}$  at 30 AU, and contain  $0.02\text{-}0.05 M_{\odot}$  of material inside 40 AU, while the standard MMSN models have  $15\text{-}40 \text{ g cm}^{-2}$  at 19 AU,  $10\text{-}25 \text{ g cm}^{-2}$  at 30 AU, and  $0.01\text{-}0.04 M_{\odot}$  inside 40 AU.

However, we should emphasize that angular resolution limitations prevent a direct characterization of the mass contents in these disks on radial scales smaller than  $\sim 20$  AU. In particular, the data cannot differentiate the assumed  $\Sigma$  formulation (§3.1) from alternative density models at smaller radii (e.g., cases where the viscosity may not be a simple power law). Therefore, since the constraints on  $\Sigma$  are made from the millimeter emission on much larger spatial scales, extrapolations of the density profiles into the inner giant planet region (i.e., in to 5 AU) remain speculative. We do find a notable difference between the sample disks and MMSN mass contents at large radii. The solar system has a relatively sharp edge at  $\sim 40$  AU (Luu & Jewitt 2002), while the sample



disks have substantial mass reservoirs on larger scales. The MMSN disk could have been externally truncated, from an encounter with a passing star (Ida et al. 2000) or an intense radiation field (Johnstone et al. 1998) in a now-dispersed massive star cluster.

In planet formation models based on the canonical “core accretion” scenario, a scaled-up MMSN disk can produce giant planets on timescales of  $\sim 3\text{--}8$  Myr (Pollack et al. 1996; Inaba et al. 2003; Hubickyj et al. 2005; Lissauer & Stevenson 2007), roughly consistent with the upper bound on disk lifetimes (e.g., Haisch et al. 2001). But Alibert et al. (2005) demonstrated that those formation timescales are reduced to only  $\sim 1$  Myr if nominal viscous evolution and migration effects are included in such calculations. Moreover, the ability to form planets in the core accretion scenario does not appear to be significantly different for  $\Sigma$  profiles that are flatter than the MMSN (like the  $\gamma \approx 0.9$  profiles inferred here), provided that there is sufficient mass in the inner disk (Wetherill 1996; Chambers & Cassen 2002; Raymond et al. 2005). Alternatively, the “disk instability” scenario can potentially form giant protoplanets via the fragmentation of a scaled-up MMSN disk on timescales as short as  $\sim 1000$  yr (Cameron 1978; Boss 1997; Mayer et al. 2007; Durisen et al. 2007). But both of these planet formation scenarios require surface densities  $\geq 2\text{--}5\times$  larger than those found for the sample disks or the MMSN, either to accommodate key timescale constraints (core accretion) or to maintain a gravitationally unstable structure (disk instability). Assuming that those requirements are accurate, it is worthwhile to consider ways to reconcile this  $\Sigma$  discrepancy.

Perhaps the most straightforward way to do that is associated with the disk opacities ( $\kappa$ ). Because the millimeter emission from a disk is related to the product  $\kappa\Sigma$ , changes to the dust opacities would be reflected in the inferred surface densities. The opacities regulate the conversion of surface brightnesses to surface densities, with an exchange rate set by the properties and size distribution of disk solids (e.g., Beckwith & Sargent 1991). The disk structures we mean to compare with planet formation models were determined for a dust grain size distribution  $n(a) \propto a^{-3.5}$  up to a maximum  $a = 1$  mm (see §3.2), and assuming that the dust tracks 1% of the total mass budget (the remainder is molecular gas). But different size distributions tend to produce *lower* millimeter opacities, which could in turn lead us to infer *higher* surface densities from the same data (Miyake & Nakagawa 1993; D’Alessio et al. 2001; Draine 2006). For example, extending the same size distribution out to 1 cm particles decreases the  $870\ \mu\text{m}$  opacity by a factor of  $\sim 2.6$  (D’Alessio et al. 2001), and would scale our  $\Sigma$  estimates up to be in line with the planet formation model requirements without dramatically affecting the estimates of other structure parameters. Such modest adjustments to the particle population are not unreasonable considering the results of grain growth simulations (Weidenschilling et al. 1997; Dullemond & Dominik 2005; Garaud 2007) and the emission signatures of centimeter-scale grains in similar disks (Natta et al. 2004; Wilner et al. 2005; Rodmann et al. 2006). Indeed, the core accretion models assume that a large population of planetesimals is already present in these disks, implying that the dust we observe is merely collisional debris (e.g., Kenyon & Bromley 2009).

Therefore, with only small modifications to the model assumptions we can conclude that the giant planet formation process is indeed feasible for the disks in this sample. In fact, planet

formation may have already started in the disks around SR 21, WSB 60, and DoAr 44. The ring-like morphology of the millimeter emission from those disks could be the signature of a low-density cavity on size scales comparable to the solar system. While a variety of mechanisms could produce this kind of structure (see D’Alessio et al. 2005; Najita et al. 2007), perhaps the most compelling is the presence of a giant planet just inside the ring edge. A sufficiently massive planet can open a gap in the disk structure, significantly decreasing (or even halting) the mass flow through to the inner disk (e.g., Lin & Papaloizou 1986; Bryden et al. 1999; Lubow et al. 1999; Lubow & D’Angelo 2006; Varnière et al. 2006). Consequently, accretion depletes the inner disk densities and diminishes the millimeter emission interior to the planet. But why might planets have formed in these three disks, and not the other six in this sample? Perhaps they formed planets early, when densities were high enough to facilitate the gravitational instability scenario. Or maybe they have simply had more time than the others to form a giant planet with the core accretion scenario: we find stellar ages of 3-7 Myr for these cases (Table 3). While individual stellar age estimates are plagued with uncertainty (Hillenbrand & White 2004), it is interesting to note that the host stars for all of the confirmed “transition” disks – with resolved images of their cavities – seem to be older than a few Myr (e.g., Piétu et al. 2006; Brown et al. 2008, 2009; Hughes et al. 2007, 2009).

## 6. Summary

We have presented the results of a high angular resolution ( $0''.3 \approx 40$  AU) survey of the  $870 \mu\text{m}$  continuum emission from 9 young circumstellar dust disks in the Ophiuchus star-forming region. Those observations were used to model some of the key size scales and physical conditions in these disks, based on two-dimensional Monte Carlo radiative transfer calculations. We find the following:

1. For a parametric surface density profile  $\Sigma \propto (R/R_c)^{-\gamma} \exp[-(R/R_c)^{2-\gamma}]$ , the radial  $\Sigma$  gradients derived for the sample disks lie in a narrow range around a median value  $\gamma = 0.9$  (from  $\gamma = 0.4$ -1.0). Therefore, the shapes of the surface density profiles for these disks are similar, varying roughly inversely with radius in the inner disk ( $\Sigma \propto 1/R$  when  $R \lesssim R_c$ ) and smoothly merging into a steeper exponential decrease at larger radii ( $\Sigma \propto 1/e^R$  when  $R \gtrsim R_c$ ). The characteristic radii that mark that transition in the  $\Sigma$  profile lie in the range  $R_c \approx 20$ -200 AU. Because these disks were selected to have bright millimeter emission, the sample is biased toward high disk masses,  $M_d \approx 0.005$ -0.14  $M_\odot$ . A variety of vertical structures are also determined, from significantly flared to nearly flat geometries.
2. These structure constraints are used to help characterize the viscous properties of the disk material. The inferred  $\gamma$  values are lower than expected for gravitationally unstable disk models ( $\gamma \approx 1.5$ ; e.g., Vorobyov & Basu 2009), but are generally consistent with simple models that incorporate a prescription for turbulent disk viscosities ( $\gamma \approx 1$ ; e.g., Hartmann et al. 1998). Combining these disk structures with accretion rate measurements and a simple viscous disk model, we estimate turbulent viscosity parameters in the range  $\alpha \approx 0.0005$ -0.08.

3. Disk densities in the outer giant planet region ( $R \approx 20\text{-}40$  AU) are comparable to the expected values for the reconstructed density structure of the primordial solar disk (MMSN), despite their generally less steep  $\Sigma$  profiles in the inner disk. But unlike the typical models of the MMSN, the sample disks have substantial mass reservoirs at large distances from the star ( $R > 40$  AU). Although current planet formation models need at least  $2\text{-}5\times$  higher densities to operate efficiently, we argue that small modifications to our assumed opacities that are consistent with modest dust grain growth can easily accommodate those model requirements.
4. Three of the sample disks (SR 21, WSB 60, and DoAr 44) exhibit resolved ring morphologies, where the continuum emission is significantly diminished inside a radius of  $\sim 20\text{-}40$  AU. A variety of mechanisms could potentially decrease densities or opacities on these scales in the inner disk, and should be explored in more detail for these cases. One interesting possibility is that these disks have already produced massive planets just inside their ring edges.

We thank Michiel Hogerheijde for kindly providing access to the 2-D version of the RATRAN code package, Paola D’Alessio for calculating various opacity spectra on our behalf, Andrea Isella for sharing results with us prior to publication, and an anonymous referee for a thoughtful and very useful review. The SMA is a joint project between the Smithsonian Astrophysical Observatory and the Academia Sinica Institute of Astronomy and Astrophysics and is funded by the Smithsonian Institution and the Academia Sinica. Support for this work was provided by NASA through Hubble Fellowship grant HF-01203.01-A awarded by the Space Telescope Science Institute, which is operated by the Association of Universities for Research in Astronomy, Inc., for NASA, under contract NAS 5-26555. D. J. W. acknowledges support from NASA Origins Grant NNG05GI81G.

### A. Accretion Disks

This appendix is intended to facilitate a clear comparison between our parametric structure models (§3) and the properties of viscously evolving accretion disks (as presented by Hartmann et al. 1998). The evolution of the density structure of a viscous disk in Keplerian rotation around a central star is characterized with the partial differential equation

$$\frac{\partial \Sigma}{\partial t} = \frac{3}{R} \frac{\partial}{\partial R} \left[ R^{1/2} \frac{\partial}{\partial R} (R^{1/2} \nu \Sigma) \right], \quad (\text{A1})$$

where  $\nu$  denotes the viscosity (Lynden-Bell & Pringle 1974; Pringle 1981). If the viscosities do not change with time and are spatially distributed as a power-law,  $\nu \propto R^\gamma$ , there is an analytic similarity solution to (A1) with the form

$$\Sigma = \frac{\mathcal{C}}{3\pi\nu_1} \left( \frac{R}{R_1} \right)^{-\gamma} \mathcal{T}^{-(5/2-\gamma)/(2-\gamma)} \exp \left[ - \left( \frac{R}{R_1} \right)^{2-\gamma} \mathcal{T}^{-1} \right], \quad (\text{A2})$$

where  $R_1$  is a scaling radius,  $\nu_1 = \nu(R_1)$ , and  $\mathcal{T}$  is a dimensionless time parameter such that  $\mathcal{T} = 1 + t/t_s$ , where  $t_s$  is the viscous timescale. Note that  $\mathcal{T} - 1$  is equivalent to the number of viscous timescales that have elapsed since the evolution began ( $t = 0$ ). The constant  $\mathcal{C}$  can be recast in terms of an initial disk mass,  $M_{d,0}$ , by integrating (A2) over the disk area at  $t = 0$  ( $\mathcal{T} = 1$ )

$$\mathcal{C} = \frac{3(2 - \gamma)\nu_1}{2R_1^2} M_{d,0} \quad (\text{A3})$$

leading to a simplified form for the surface density profile in (A2)

$$\Sigma = (2 - \gamma) \left( \frac{M_{d,0}}{2\pi R_1^2} \right) \mathcal{T}^{-(5/2-\gamma)/(2-\gamma)} \left( \frac{R}{R_1} \right)^{-\gamma} \exp \left[ - \left( \frac{R}{R_1} \right)^{2-\gamma} \mathcal{T}^{-1} \right]. \quad (\text{A4})$$

This  $\Sigma$  profile resembles the parametric form used in our models

$$\Sigma = (2 - \gamma) \left( \frac{M_d}{2\pi R_c^2} \right) \left( \frac{R}{R_c} \right)^{-\gamma} \exp \left[ - \left( \frac{R}{R_c} \right)^{2-\gamma} \right] \quad (\text{A5})$$

where equations (4) and (5) in §3.1 have been combined to ease the comparison. The radial behavior of the exponential surface density tapers in (A4) and (A5) are identical if

$$R_c = R_1 \mathcal{T}^{1/(2-\gamma)} \quad (\text{A6})$$

as described in equation (7) of §5.1. Inserting that relation back into (A4) and comparing with (A5) confirms the evolutionary behavior of the disk mass derived by Hartmann et al. (1998, their equation 26) and noted in equation (8) of §5.1,

$$M_d = M_{d,0} \mathcal{T}^{-1/2(2-\gamma)}. \quad (\text{A7})$$

Some additional insight can be inferred from the behavior of the mass flow rate

$$\dot{M} = \mathcal{C} \mathcal{T}^{-(5/2-\gamma)/(2-\gamma)} \left[ 1 - \frac{2(2-\gamma)}{\mathcal{T}} \left( \frac{R}{R_1} \right)^{2-\gamma} \right] \exp \left[ - \left( \frac{R}{R_1} \right)^{2-\gamma} \mathcal{T}^{-1} \right] \quad (\text{A8})$$

for these viscous disk models (Hartmann et al. 1998, their equation 21). To conserve angular momentum, the direction of the mass flow (i.e., the sign of  $\dot{M}$ ) changes at a radius

$$R_t = R_1 \left[ \frac{\mathcal{T}}{2(2-\gamma)} \right]^{1/(2-\gamma)} = R_c \left[ \frac{1}{2(2-\gamma)} \right]^{1/(2-\gamma)} \quad (\text{A9})$$

such that the bulk flow is in toward the star ( $\dot{M} > 0$ ) when  $R < R_t$ , and outwards to larger radii in the disk ( $\dot{M} < 0$ ) when  $R > R_t$ . The second relation in (A9), obtained using (A6), demonstrates that the model parameters  $\{\gamma, R_c\}$  provide important constraints on the mass flow in the disk. The only other available mass flow diagnostics are the accretion rates onto the star,  $\dot{M}_*$ . Substituting

in (A3), (A6), and (A7), and recognizing that  $\dot{M}_*$  corresponds to the value of  $\dot{M}$  at very small radii ( $R \ll R_c$ ), (A8) can be written in the form

$$\dot{M}_* \approx \frac{3(2-\gamma)}{2} \nu_1 \left( \frac{M_d}{R_c^2} \right) \mathcal{T}^{\gamma/(2-\gamma)}. \quad (\text{A10})$$

This relation suggests that some of the key disk structure parameters that can be constrained observationally,  $\{M_d, \gamma, R_c, \dot{M}_*\}$ , are potential probes of the disk viscosities (i.e.,  $\nu_1$ ).

In a typical parameterization for accretion disks (Shakura & Sunyaev 1973), the viscosity is proportional to the product of the sound speed ( $c_s$ ) and scale height ( $H$ )

$$\nu = \alpha c_s H = \nu_1 \left( \frac{R}{R_1} \right)^\gamma \quad (\text{A11})$$

with the proportionality constant  $\alpha$  considered a diagnostic for the efficiency of angular momentum transport. Here, the second equality is the definition of the viscosity for the similarity solutions in (A2). Rearranging (A11) and substituting (A6) for  $R_1$  gives

$$\nu_1 = \alpha c_s H \left( \frac{R}{R_c} \right)^{-\gamma} \mathcal{T}^{-\gamma/(2-\gamma)}, \quad (\text{A12})$$

which can be substituted into (A10) to solve for  $\alpha$ ,

$$\alpha \approx \frac{2R_c^2}{3(2-\gamma)} \frac{\dot{M}_*}{M_d} \left( \frac{R}{R_c} \right)^\gamma \frac{1}{c_s H} = \frac{\dot{M}_*}{3\pi\Sigma_c} \left( \frac{R}{R_c} \right)^\gamma \frac{1}{c_s H} \quad (\text{A13})$$

where the second equality has utilized equation (5) in §3.1. This form in (A13) is identical to equation (10) in §5.1 (see also Hartmann et al. 1998, their equation 22).

Based on (A13) the value of  $\alpha$  varies with radius proportional to  $R^\gamma/c_s H$ . Following equation (3) in §3.1, the scale heights vary as  $H \propto R^{1+\psi}$ . We can approximate the sound speed variation as  $c_s \propto \sqrt{T}$ , where  $T$  is evaluated at the midplane. Given the power-law temperature profiles found in §4.1.4 (see Fig. 10),  $c_s \propto R^{-q/2}$ . Therefore,  $\alpha$  has a power-law dependence on radius,  $\alpha \propto R^z$  with  $z = \gamma + 0.5q - \psi - 1$ . For the disks in this sample,  $z$  is generally small ( $< 0.1$ ) but can range from  $-0.4$  (AS 209) to  $0.3$  (WaOph 6). At most,  $\alpha$  varies by an order of magnitude across the disk, although typically it is constant within a factor of  $\sim 2$ -3.

Table 1. SMA Observing Journal

Name (1)	$\alpha$ [J2000] (2)	$\delta$ [J2000] (3)	Array (4)	UT Date (5)	Alt. Name (6)
AS 205	16 11 31.35	–18 38 26.0	V	2007 June 17	V866 Sco, HBC 254
			V	2007 May 26	
			E	2006 June 3	
			C	2006 May 12	
GSS 39	16 26 45.03	–24 23 08.0	V	2008 April 5	Elias 27
			C	2006 May 14	
AS 209	16 49 15.29	–14 22 08.8	V	2007 June 9	V1121 Oph, HBC 270
			E	2006 June 3	
			C	2006 May 12	
DoAr 25	16 26 23.69	–24 43 14.1	V	2007 June 17	YLW 34
			V	2007 May 26	
			C	2005 June 12	
			E	2005 May 8	
WaOph 6	16 48 45.62	–14 16 36.0	V	2007 June 9	V2508 Oph, HBC 653
			C	2005 June 12	
			E	2005 May 15	
SR 21	16 27 10.27	–24 19 12.8	V	2007 June 10	Elias 30
			S	2008 August 29	
VSSG 1	16 26 18.87	–24 28 19.9	C	2008 May 13	Elias 20
			V	2008 April 5	
WSB 60	16 28 16.51	–24 36 58.3	C	2008 May 13	YLW 58
			V	2008 April 3	
DoAr 44	16 31 33.46	–24 27 37.4	C	2008 May 13	Haro 1-16, ROXs 44
			V	2008 April 3	

Note. — Col. (1): Disk name. Cols. (2) & (3): Centroid coordinates, determined as described in the text (§2). Col. (4): Array configuration; V = very extended (68-509 m baselines), E = extended (28-226 m baselines), C = compact (16-70 m baselines), and S = sub-compact (6-70 m baselines). Col. (5): UT date of observation. Observations prior to 2007 were described by Andrews & Williams (2007a), and the archival SR 21 V data were originally presented by Brown et al. (2009). Col. (6): Common alternative identifications.

Table 2. Continuum and CO  $J=3-2$  Synthesized Map Properties

Disk	continuum				CO $J=3-2$		
	$\lambda_{\text{eff}}$ [ $\mu\text{m}$ ]	$F_{\nu}$ [mJy]	$\theta_b$ [ $''$ ]	PA $_b$ [ $^{\circ}$ ]	rms [Jy]	$\theta_b$ [ $''$ ]	PA $_b$ [ $^{\circ}$ ]
(1)	(2)	(3)	(4)	(5)	(6)	(7)	(8)
AS 205	859	$960 \pm 7$	$0.46 \times 0.37$	22	0.25	$2.19 \times 1.60$	176
GSS 39	882	$663 \pm 3$	$0.63 \times 0.54$	26	0.50	$3.26 \times 1.80$	168
AS 209	859	$577 \pm 3$	$0.56 \times 0.45$	36	0.25	$2.38 \times 1.73$	176
DoAr 25	865	$563 \pm 3$	$0.45 \times 0.34$	15	0.22	$1.80 \times 1.43$	178
WaOph 6	869	$405 \pm 3$	$0.49 \times 0.38$	37	0.20	$1.61 \times 1.44$	177
SR 21	865	$371 \pm 2$	$0.50 \times 0.36$	17	0.13	$3.07 \times 2.03$	3
VSSG 1	882	$275 \pm 2$	$0.46 \times 0.30$	31	0.22	$2.36 \times 1.32$	47
WSB 60	883	$255 \pm 3$	$0.58 \times 0.38$	25	0.38	$2.96 \times 2.42$	31
DoAr 44	883	$229 \pm 3$	$0.57 \times 0.35$	23	0.26	$2.29 \times 1.35$	47

Note. — Col. (1): Disk name. Col. (2): Effective wavelength of the combined continuum data. Col. (3): Integrated continuum flux density and rms noise in the map (does not include the  $\sim 10\%$  flux calibration uncertainty). Cols. (4) & (5): FWHM dimensions and position angle (measured east of north) of the synthesized beam for the continuum maps shown in Figure 1. Note that the SR 21 images were generated for a different visibility weighting (robust = 0.3, compared to 0.7 for the rest of the sample). Col. (6): The rms noise level per beam for an individual channel in the synthesized channel maps. For AS 205 and AS 209, the channel width is  $0.18 \text{ km s}^{-1}$ , for SR 21 it is  $0.44 \text{ km s}^{-1}$ , and for the others it is  $0.70 \text{ km s}^{-1}$ . Cols. (7) & (8): FWHM dimensions and position angle of the synthesized beam for the CO channel maps.

Table 3. Stellar Properties

Name	SpT	$A_V$	$T_{\text{eff}}$	$R_*$	$L_*$	$M_*$	age	ref
(1)	(2)	[mag]	[K]	[ $R_\odot$ ]	[ $L_\odot$ ]	[ $M_\odot$ ]	[Myr]	(9)
AS 205	K5	2.9	4250	3.7	4.0	1.0	0.5	1
GSS 39	M0	15	3850	2.3	1.0	0.6	1.0	2
AS 209	K5	0.9	4250	2.3	1.5	0.9	1.6	3
DoAr 25	K5	2.7	4250	1.7	0.8	1.0	3.8	4
WaOph 6	K6	3.6	4205	3.2	2.9	0.9	0.7	5
SR 21	G3	6.3	5800	3.3	11	2.0	4.7	1
VSSG 1	M0	14	3850	3.1	1.9	0.6	0.7	6
WSB 60	M4	3.5	3370	1.3	0.2	0.3	3.0	4
DoAr 44	K3	2.3	4730	1.7	1.3	1.4	7.1	7

Note. — Col. (1): Disk name. Col. (2): Spectral type. Col. (3): Visual extinction. Col. (4): Effective temperature. Col. (5): Stellar radius. Col. (6): Stellar luminosity. Col. (7) and (8): Stellar mass and age estimated from the Siess et al. (2000) pre-main-sequence models. Col. (9): Literature references for SpT and  $A_V$ : [1] - Prato et al. (2003), [2] - Luhman & Rieke (1999), [3] - Herbig & Bell (1988), [4] - Wilking et al. (2005), [5] - Eisner et al. (2005), [6] - Natta et al. (2006), [7] - Bouvier & Appenzeller (1992).



Table 4. Disk Structure Model Parameters: Continuous Cases

Name	$M_d$ [ $M_\odot$ ]	$\gamma$	$R_c$ [AU]	$H_{100}$ [AU]	$\psi$	$R_{\text{in}}$ [AU]	$i$ [ $^\circ$ ]	PA [ $^\circ$ ]	$\tilde{\chi}_{\text{vis}}^2$	$\tilde{\chi}_{\text{sed}}^2$
(1)	(2)	(3)	(4)	(5)	(6)	(7)	(8)	(9)	(10)	(11)
AS 205	0.029	0.9	46	19.6	0.11	0.14	25	165	2.1	3.7
GSS 39	0.143	0.7	198	7.3	0.08	0.07	60	110	1.9	32
AS 209	0.028	0.4	126	13.3	0.10	0.09	38	86	1.7	2.4
DoAr 25	0.136	0.9	80	6.7	0.15	0.06	59	112	1.9	9.2
WaOph 6	0.077	1.0	153	4.4	0.06	0.12	39	171	1.8	1.8
VSSG 1	0.029	0.8	33	9.7	0.08	0.10	53	165	1.8	12

Note. — Col. (1): Disk name. Col. (2): Disk mass assuming a 100:1 gas-to-dust mass ratio. Col. (3): Radial surface density gradient (eqn. 4). Col. (4): Characteristic radius (eqns. 3-4). Col. (5): Scale height at 100 AU (eqn. 2). Col. (6): Radial scale height gradient (eqn. 3). Col. (7): Fixed inner disk radius (eqn. 6). Col. (8): Fixed disk inclination (see §3.2). Col. (9): Fixed major axis position angle (see §3.2). Col. (10): Reduced  $\chi^2$  statistic ( $\chi^2$  divided by the number of degrees of freedom) comparing the model fit with the continuum visibilities alone. Col. (11): Same as Col. (10), but for the SED alone.

Table 5. Disk Structure Model Parameters: Central Cavity Cases

Name	$M_d$ [ $M_\odot$ ]	$\gamma$	$R_c$ [AU]	$H_{100}$ [AU]	$\psi$	$R_{\text{cav}}$ [AU]	$\delta_{\text{cav}}$	$i$ [ $^\circ$ ]	PA [ $^\circ$ ]	$\tilde{\chi}_{\text{vis}}^2$	$\tilde{\chi}_{\text{sed}}^2$
(1)	(2)	(3)	(4)	(5)	(6)	(7)	(8)	(9)	(10)	(11)	(12)
SR 21	0.005	0.9	17	7.7	0.26	37	0.005	22	110	1.7	7.2
WSB 60	0.021	0.8	31	11.0	0.13	20	0.01	25	117	1.8	3.0
DoAr 44	0.017	1.0	80	3.5	0.04	33	0.0001	45	75	1.8	...

Note. — Cols. (1-6): Same as for Table 4. Col. (7): The cavity radius, marking the outer edge of the diminished inner disk densities (see §3.1 and §4.1.5). Col. (8): The density reduction scaling factor inside the radius  $R_{\text{cav}}$  (see §3.1 and §4.1.5). Cols. (9-12): Same as for Table 4 cols. (8-11).

Table 6. Viscous Disk Properties

Name	$\dot{M}_*$ [ $M_\odot \text{ yr}^{-1}$ ]	ref	$R_t$ [AU]	$\alpha$	$R_1$ [AU]		$M_{d,0}$ [ $M_\odot$ ]	
(1)	(2)	(3)	(4)	(5)	(6)	(7)	(8)	(9)
AS 205	$8 \times 10^{-8}$	1	23	0.005	24	5	0.040	0.090
GSS 39	$7 \times 10^{-8}$	2	95	0.03	115	30	0.189	0.370
AS 209	$9 \times 10^{-8}$	3	61	0.08	81	27	0.035	0.061
DoAr 25	$3 \times 10^{-9}$	4	39	0.0005	43	9	0.187	0.407
WaOph 6	$1 \times 10^{-7}$	5	78	0.05	74	12	0.110	0.269
VSSG 1	$1 \times 10^{-7}$	2	16	0.02	18	4	0.039	0.079
SR 21	$< 2 \times 10^{-9}$	2	9	...	9	2	0.007	0.015
WSB 60	$2 \times 10^{-9}$	2	15	...	18	5	0.027	0.054
DoAr 44	...	...	40	...	40	7	0.023	0.055

Note. — Col. (1): Disk name. Col. (2): Mass accretion rate. Col. (3): Literature references for  $\dot{M}_*$ : [1] - Prato et al. (2003), [2] - Natta et al. (2006), [3] - Johns-Krull et al. (2000), [4] - Luhman & Rieke (1999), [5] - Eisner et al. (2005). Col. (4): Radius marking where the mass flow changes direction, based on equation (9). Col. (5): Viscosity parameter, based on equation (10). Col. (6): Initial radius encircling  $\sim 60\%$  of the disk mass if 1 viscous timescale has elapsed ( $\mathcal{T} = 2$ ), based on equation (7) (see Fig. 11). Col. (7): Same as Col. (6), but for the case where 10 viscous timescales have elapsed ( $\mathcal{T} = 11$ ). Col. (8): Initial disk mass if 1 viscous timescale has elapsed ( $\mathcal{T} = 2$ ), based on equation (8) (see Fig. 11). Col. (9): Same as Col. (8), but for the case where 10 viscous timescales have elapsed ( $\mathcal{T} = 11$ ).

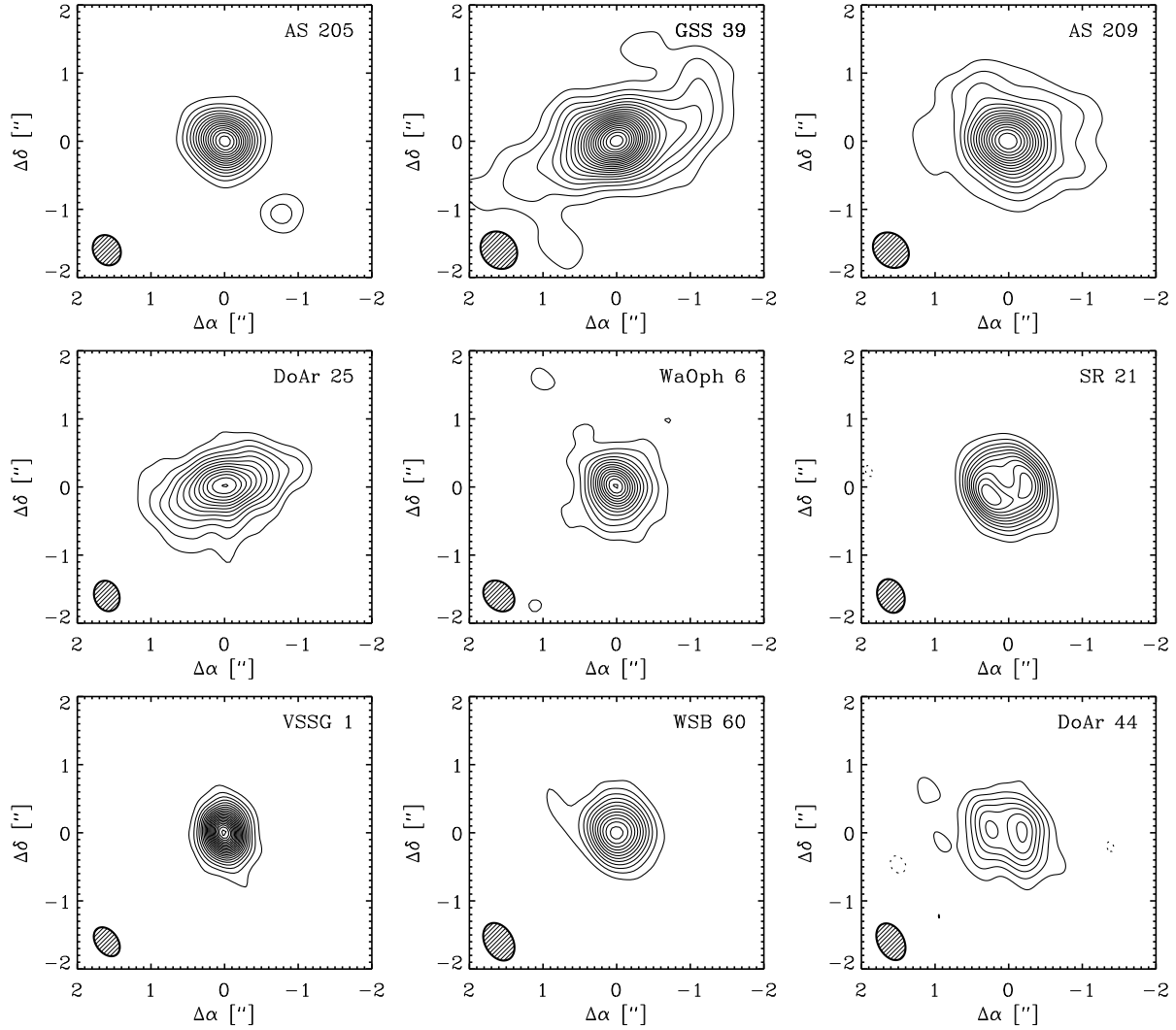


Fig. 1.— Aperture synthesis images of the  $870\ \mu\text{m}$  continuum emission from the 9 sample disks. Each panel is  $4''$  (500 AU) on a side. Contours are shown at  $3\sigma$  intervals (rms uncertainties in Table 2). The synthesized beams are shown in the lower left of each panel. Note the detection of a disk around the AS 205 B system in the top left panel (see §4.2), as well as the prominent cleared central regions for the disks around SR 21 and DoAr 44.

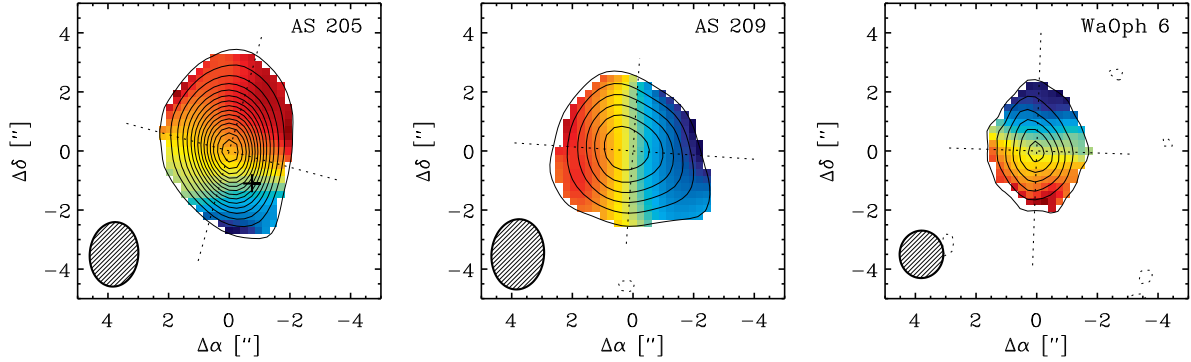


Fig. 2.— Moment maps of the CO  $J=3-2$  emission from the sample disks with minimal contamination from the surrounding molecular cloud. Each panel is  $10''$  (1250 AU) on a side. The contours mark the velocity-integrated intensity (zeroth moment), with levels at  $3\sigma$  intervals. The color-scale maps represent the intensity-weighted velocities (first moment), ranging from LSR velocities of  $3-5 \text{ km s}^{-1}$  for AS 205,  $-3-0 \text{ km s}^{-1}$  for AS 209, and  $-3-1 \text{ km s}^{-1}$  for WaOph 6. The synthesized beams are shown in the lower left of each panel. The location of AS 205 B is marked with a cross.

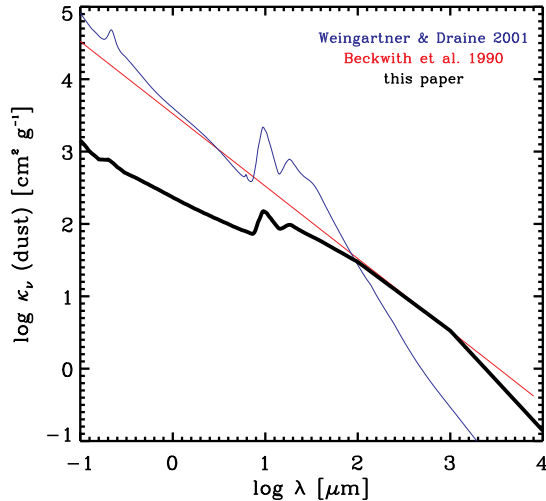


Fig. 3.— The opacity spectrum for the dust grain population adopted in the modeling (*black*). For comparison, we show the opacities for the standard Beckwith et al. (1990) prescription for disks (*red*) and the diffuse interstellar medium (*blue*; Weingartner & Draine 2001).

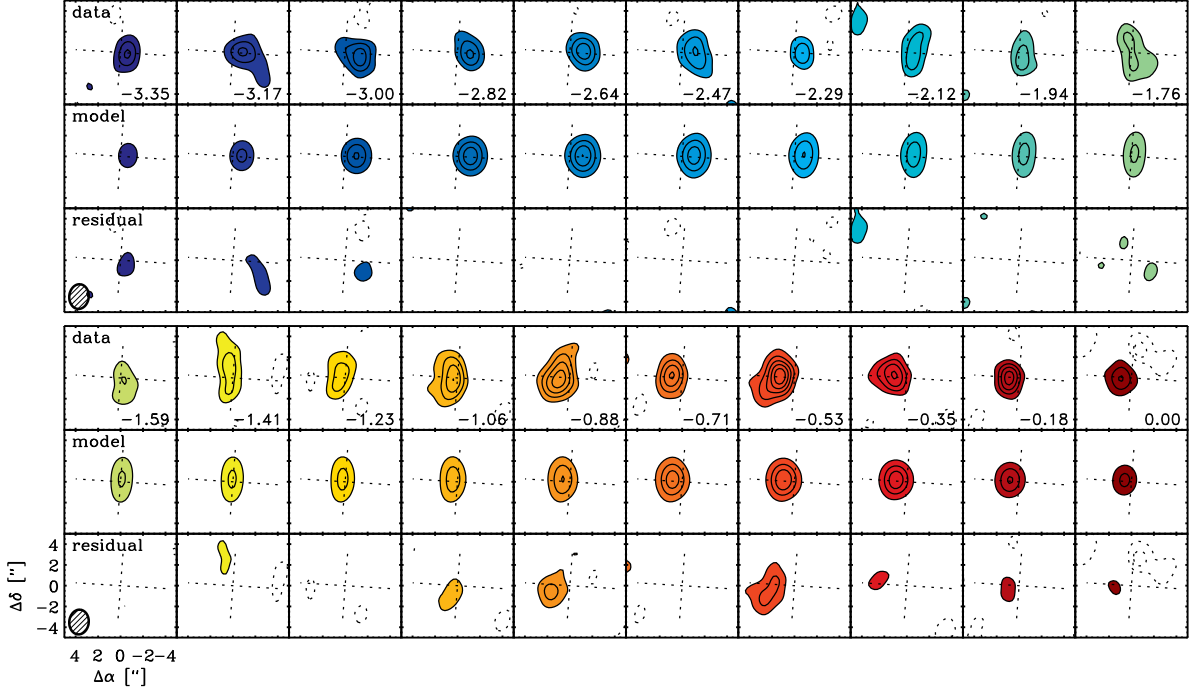


Fig. 4.— CO  $J=3-2$  channel maps for the AS 209 disk. Each panel is  $10''$  (1250 AU) on a side and represents a velocity width of  $0.18 \text{ km s}^{-1}$ , as marked in the lower right corner. Contours are shown at  $3\sigma$  intervals. The data are shown in the top rows (first and fourth), the best-fit model (see §3.2) in the middle rows (second and fifth), and the residuals in the bottom rows (third and sixth). These CO data were used only to constrain the viewing geometry of the disk.

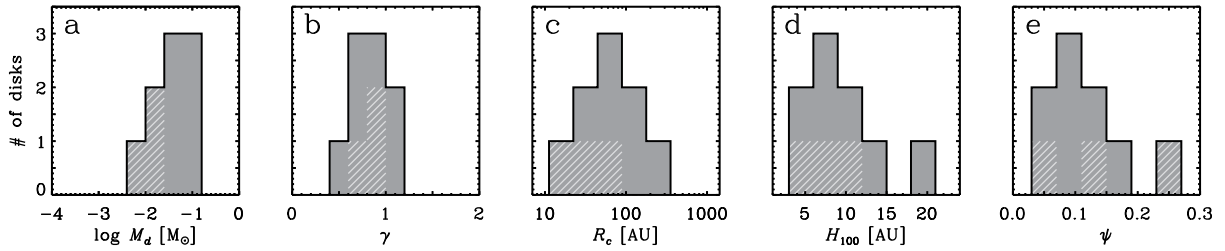


Fig. 5.— Distributions of the five key structure parameters derived for the disks in this sample. From left to right are the disk masses ( $M_d$ ), radial surface density gradients ( $\gamma$ ), characteristic radii ( $R_c$ ), scale heights at 100 AU ( $H_{100}$ ; i.e.,  $h_c$ ), and the radial scale height gradients ( $\psi$ ). The contributions of the three disks with cleared central cavities are overlaid with hatched regions.

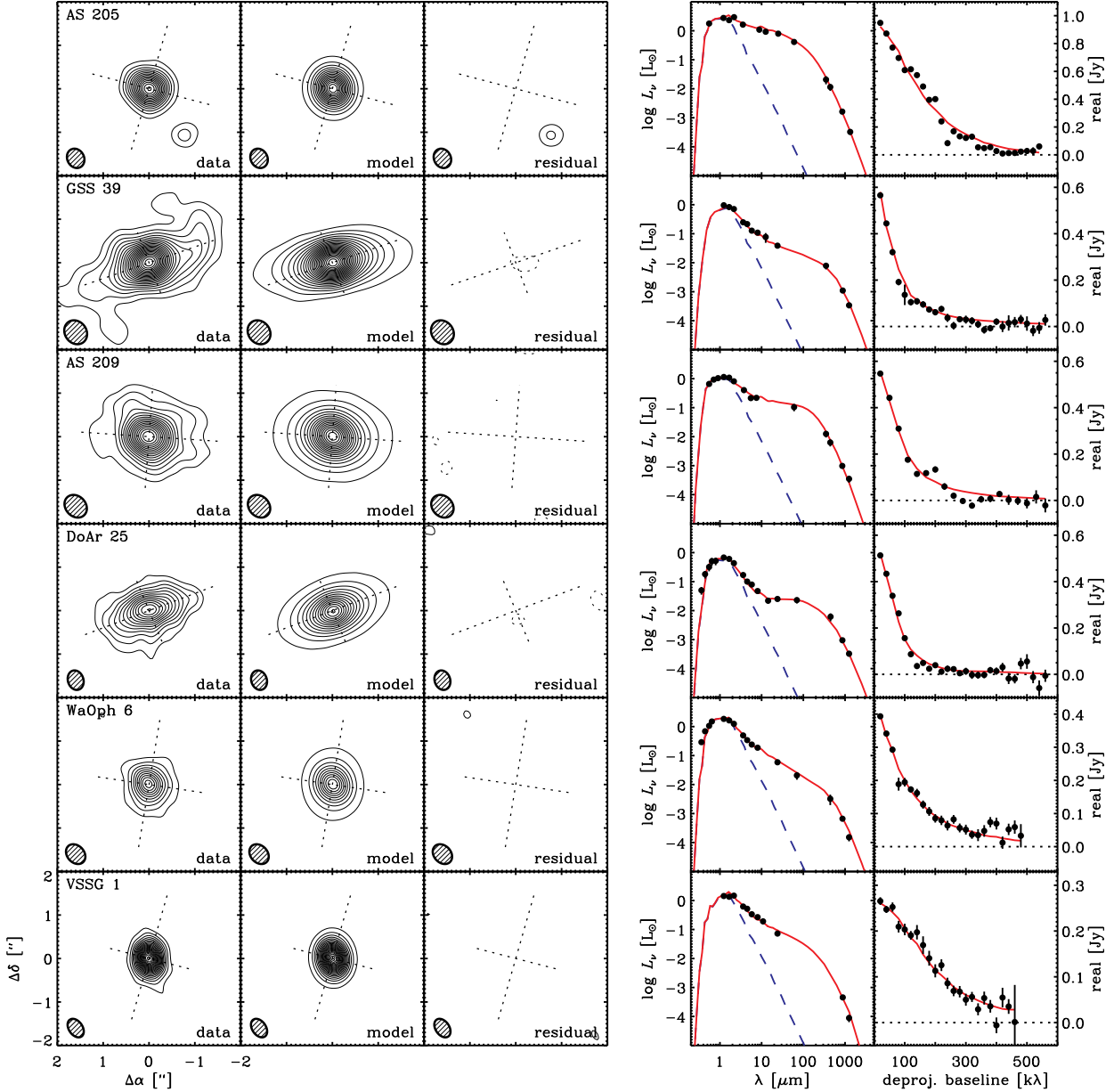


Fig. 6.— Comparison of the disk structure model fits and the data. The left panels show the SMA continuum image, corresponding disk model, and residuals (data–model) as described in Figure 1. Crosshairs mark the disk centers and major axis position angle; their relative lengths represent the disk inclination. The right panels show the broadband SEDs and deprojected visibility profiles (see §4.1 for details), with best-fit models overlaid in red. The SED contributions from the stellar photosphere are shown as blue dashed curves.

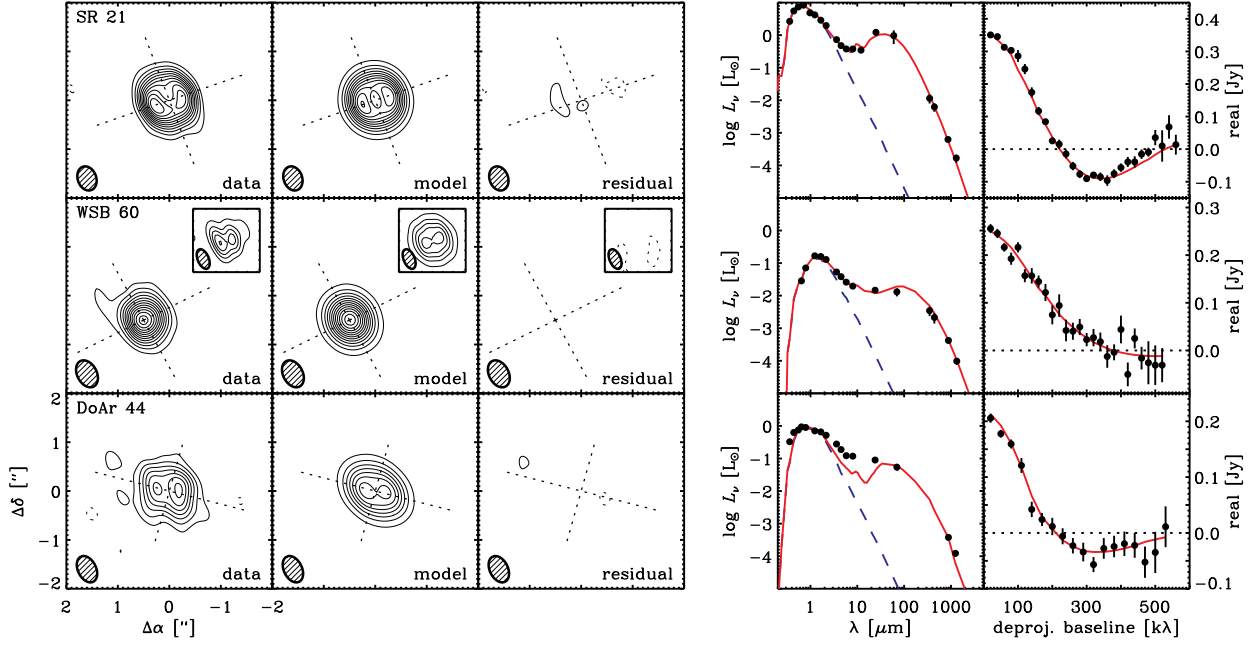


Fig. 7.— Comparison of the disk structure model fits and the data for the three cases with significantly diminished emission in their central regions. The panels are as in Figure 6, although note the slightly different bin sizes ( $30\text{ k}\lambda$ ) for the DoAr 44 visibility profile. High resolution inset images are constructed for the WSB 60 disk, showing (to scale) the detailed structure of the continuum emission on the smallest spatial scales. Each inset is  $1''.3$  ( $\sim 160\text{ AU}$ ) on a side, centered on the continuum peak in the main image (which is intentionally offset there for clarity). Contour levels in the inset are at intervals of  $10\text{ mJy beam}^{-1}$ . Only a crude inner hole model is used here; more detailed examination of the emission morphologies and SEDs will be made elsewhere.

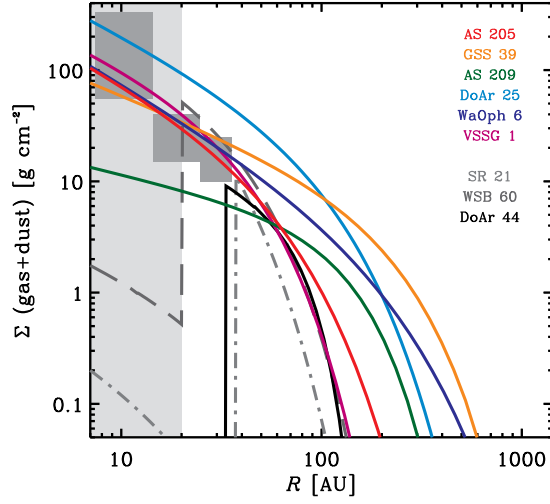


Fig. 8.— Radial surface density (gas+dust) profiles derived for the sample disks, based on the parameters in Tables 4 and 5 and equations (4) and (5). The three disks with central emission cavities are shown with grayscale curves (SR 21 as *dash-dot*, WSB 60 as *long-dash*, and DoAr 44 as *solid*). The dark gray rectangular regions mark the surface densities for Saturn, Uranus, and Neptune in the Minimum Mass Solar Nebula, reconstructed from current planet masses augmented to solar composition and smeared into annuli (see Weidenschilling 1977, and §5). The sample disks are well-characterized by radial surface density gradients in the range  $\gamma = 0.4$ -1.0 with a median value  $\gamma = 0.9$ , and a range of masses and characteristic size scales. The light gray shaded region marks the maximum resolution scale of the SMA observations.

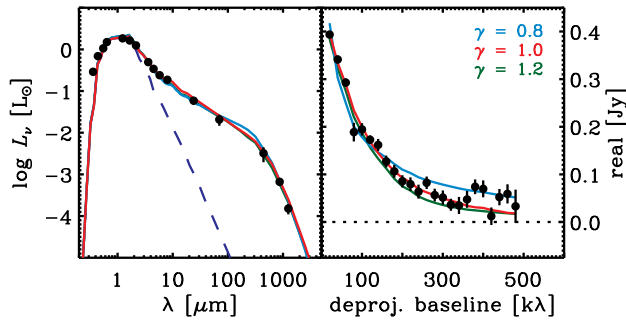


Fig. 9.— Qualitative demonstration of the accuracy in the fitted  $\gamma$  values, as discussed in §3.4. The SED (*left*) and visibility profile (*right*) are shown for the WaOph 6 disk, as in Figure 6. The red curves again show the best-fit model ( $\gamma = 1.0$ ; see Table 4), while the blue and green curves show the models that best reproduce the data for  $\gamma = 0.8$  and 1.2, respectively. While all  $\gamma$  values can reproduce the observed SED, those with departures of  $\pm 0.2$  from the best-fit  $\gamma$  value show clear differences with the millimeter visibilities.



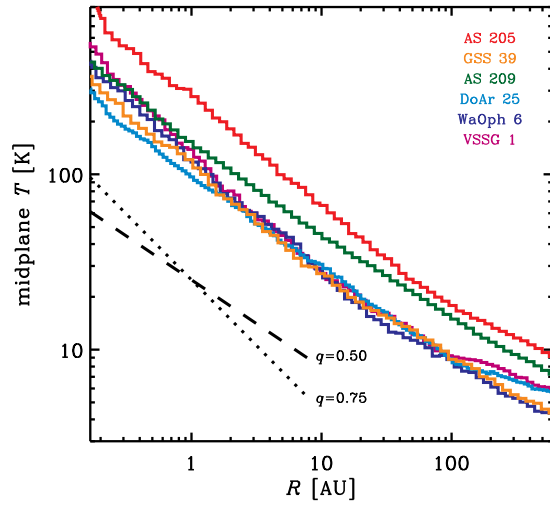


Fig. 10.— Radial dust temperature profiles at the midplane for the sample disks with continuous density distributions, determined from radiative transfer calculations (see §3.3; the disks with central cavities are excluded for clarity). The profiles are consistent with power-laws,  $T \propto R^{-q}$  with  $q \approx 0.5\text{-}0.6$ , that flatten out at large radii ( $R > R_c$ ). Some representative power-laws are shown as dashed ( $q = 0.50$ ) and dotted ( $q = 0.75$ ) lines in the lower left. The midplane temperatures are set primarily by the vertical structure of the disk (see §4.1.4).

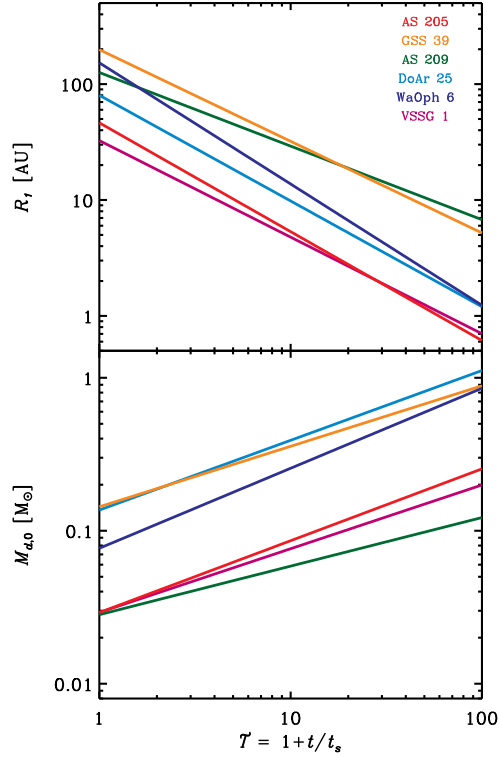


Fig. 11.— Constraints on the initial conditions for a parametric viscous disk model as a function of the unknown value of  $\mathcal{T}$  (the number of elapsed viscous timescales): (*top*) initial scaling radius from equation (7); and (*bottom*) initial disk mass from equation (8). Note that  $\{R_1, M_{d,0}\}$ , *do not vary with time* in these models. Rather, these plots show what their appropriate values would be if  $\mathcal{T} - 1$  viscous timescales have elapsed since the start of the evolution process (see Table 6). The disks with central cavities are excluded, because they have been clearly affected by additional evolutionary mechanisms.

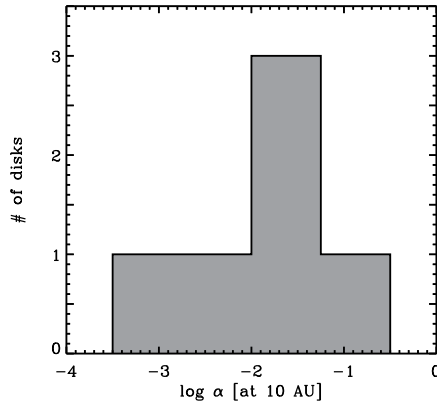


Fig. 12.— Distribution of viscosity parameters,  $\alpha$ , inferred from the structure models and accretion rates for the sample disks, based on equation (10) (see Table 6). While these values are appropriate for  $R = 10$  AU,  $\alpha$  is only weakly dependent on radius (see the Appendix).

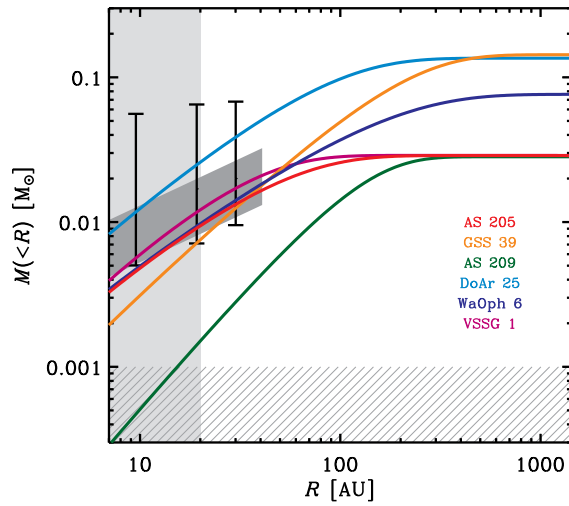


Fig. 13.— The encircled mass profiles, or cumulative mass interior to  $R$ , for the sample disks with continuous density distributions. Vertical error bars mark the range of acceptable  $M(<R)$  values for Saturn, Uranus, and Neptune in the MMSN, reflecting the uncertainties of augmenting planet masses to solar composition (including those for planets interior to these radii). The dark gray region shows the standard  $\Sigma \propto R^{-1.5}$  profiles for the MMSN with the range of normalizations adopted in the literature (Weidenschilling 1977; Hayashi 1981). There is generally good agreement between the disk structure model results and the fossil record of the mass content for the primordial disk around the Sun. The light shaded region marks the maximum resolution scale of the SMA observations, while the hatched region is an approximate representation of the  $3\sigma$  mass sensitivity of the data (assuming a typical  $T \approx 10$  K).

## REFERENCES

- Alexander, R. D., Clarke, C. J., & Pringle, J. E. 2006, *MNRAS*, 369, 216
- Alexander, R. D., & Armitage, P. J. 2007, *MNRAS*, 375, 500
- Alexander, R. 2008, *New Astronomy Reviews*, 52, 60
- Alibert, Y., Mordasini, C., Benz, W., & Winisdoerffer, C. 2005, *A&A*, 434, 343
- Akeson, R. L., Ciardi, D. R., van Belle, G. T., & Creech-Eakman, M. J. 2002, *ApJ*, 566, 1124
- André, P., & Montmerle, T. 1994, *ApJ*, 420, 837
- Andrews, S. M., & Williams, J. P. 2005, *ApJ*, 635, 1134
- 2007, *ApJ*, 659, 705 (2007a)
- 2007, *ApJ*, 671, 1800 (2007b)
- Andrews, S. M., Hughes, A. M., Wilner, D. J., & Qi, C. 2008, *ApJ*, 678, L133
- Balbus, S. A., & Hawley, J. F. 1991, *ApJ*, 376, 214
- Beckwith, S. V. W., Sargent, A. I., Chini, R. S., & Güsten, R. 1990, *AJ*, 99, 924
- Beckwith, S. V. W., & Sargent, A. I. 1991, *ApJ*, 381, 250
- Beckwith, S. V. W., Henning, T., & Nakagawa, Y. 2000, in *Protostars & Planets IV*, eds. V. Mannings, A. P. Boss, & S. S. Russell (Tucson: Univ. Arizona Press), 533
- Bjorkman, J. E., & Wood, K. 2001, *ApJ*, 554, 615
- Boss, A. P. 1997, *Science*, 276, 1836
- Bouvier, J., & Appenzeller, I. 1992, *A&AS*, 92, 481
- Brown, J. M., et al. 2007, *ApJ*, 664, L107
- 2009, in preparation
- Brown, J. M., Blake, G. A., Qi, C., Dullemond, C. P., & Wilner, D. J. 2008, *ApJ*, 675, L109
- Bryden, G., Chen, X., Lin, D. N. C., Nelson, R. P., & Papaloizou, J. C. B. 1999, *ApJ*, 514, 344
- Calvet, N., Magrit, G. C., Patino, A., & D’Alessio, P. 1992, *RMxAA*, 24, 27
- Calvet, N., Hartmann, L., & Strom, S. E. 2000, in *Protostars & Planets IV*, eds. V. Mannings, A. P. Boss, & S. S. Russell (Tucson: Univ. Arizona Press), 377

- Calvet, N., Muzerolle, J., Briceño, C., Hernández, J., Hartmann, L., Saucedo, J. L., & Gordon, K. D. 2004, *AJ*, 128, 1294
- Calvet, N., et al. 2005, *ApJ*, 630, L185
- Cameron, A. G. W. 1978, *Moon and Planets*, 18, 5
- 1988, *ARA&A*, 26, 441
- Chambers, J. E., & Cassen, P. 2002, *Meteoritics & Planetary Science*, 37, 1523
- Chiang, E. I., & Goldreich, P. 1997, *ApJ*, 490, 368
- Chiang, E. I., Joungh, M. K., Creech-Eakman, M. J., Qi, C. Kessler, J. E., Blake, G. A., & van Dishoeck, E. F. 2001, *ApJ*, 547, 1077
- Chini, R. 1981, *A&A*, 99, 346
- Clarke, C. J., Gendrin, A., & Sotomayor, M. 2001, *MNRAS*, 328, 485
- Cohen, M., & Kuhl, L. V. 1979, *ApJS*, 41, 743
- Crida, A. 2009, *ApJ*, in press
- Cutri, R. M., et al. 2003, *2MASS All-Sky Point Source Catalog* (Pasadena: IPAC)
- D’Alessio, P., Calvet, N., & Hartmann, L. 2001, *ApJ*, 553, 321
- D’Alessio, P. et al. 2005, *ApJ*, 621, 461
- D’Alessio, P., Calvet, N., Hartmann, L., Franco-Hernández, R., & Servín, H. 2006, *ApJ*, 638, 314
- Dartois, E., Dutrey, A., & Guilloteau, S. 2003, *A&A*, 399, 773
- Davis, S. S. 2005, *ApJ*, 627, L153
- de Geus, E. J., de Zeeuw, P. T., & Lub, J. 1989, *A&A*, 216, 44
- Dent, W. R. F., Matthews, H. E., & Ward-Thompson, D. 1998, *MNRAS*, 301, 1049
- Desch, S. J. 2007, *ApJ*, 671, 878
- Draine, B. T. 2006, *ApJ*, 636, 1114
- Draine, B. T., & Lee, H. M. 1984, *ApJ*, 285, 89
- Dullemond, C. P., Dominik, C., & Natta, A. 2001, *ApJ*, 560, 957
- Dullemond, C. P., & Dominik, C. 2004, *A&A*, 417, 159 (2004a)

——— 2004, *A&A*, 421, 1075 (2004b)

——— 2005, *A&A*, 434, 971

Dullemond, C. P., Hollenbach, D., Kamp, I., & D’Alessio, P. 2007, in *Protostars & Planets V*, eds. B. Reipurth, D. Jewitt, & K. Keil (Tucson: Univ. Arizona Press), 555

Durisen, R. H., Boss, A. P., Mayer, R. L., Nelson, A. F., Quinn, T., & Rice, W. K. M. 2007, in *Protostars & Planets V*, eds. B. Reipurth, D. Jewitt, & K. Keil (Tucson: Univ. Arizona Press), 607

Dutrey, A., Guilloteau, S., Prato, L., Simon, M., Duvert, G., Schuster, K., & Ménard, F. 1998, *A&A*, 338, L63

Dutrey, A., Guilloteau, S., & Simon, M. 2003, *A&A*, 402, 1003

Eisner, J. A., Hillenbrand, L. A., White, R. J., Akeson, R. L., & Sargent, A. I. 2005, *ApJ*, 623, 952

Espaillet, C., et al. 2007, *ApJ*, 670, L135

Espaillet, C., Calvet, N., Luhman, K. L., Muzerolle, J., & D’Alessio, P. 2008, *ApJ*, 682, L125

Evans, N. J., et al. 2003, *PASP*, 115, 965

Fleming, T., & Stone, J. M. 2003, *ApJ*, 585, 908

Fromang, S., Papaloizou, J., Lesur, G., & Heinemann, T. 2007, *A&A*, 476, 1123

Garaud, P. 2007, *ApJ*, 671, 2091

Ghez, A. M., Neugebauer, G., & Matthews, K. 1993, *AJ*, 106, 2005

Glauser, A. M., Ménard, F., Pinte, C., Duchêne, G., Güdel, M., Monin, J.-L., & Padgett, D. L. 2008, *A&A*, 485, 531

Grankin, K. N., Melnikov, S. Y., Bouvier, J., Herbst, W., & Shevchenko, V. S. 2007, *A&A*, 461, 183

Greene, T. P., Wilking, B. A., André, P., Young, E. T., & Lada, C. J. 1994, *ApJ*, 434, 614

Greene, T. P., & Lada, C. J. 1996, *AJ*, 112, 2184

Guenther, E. W., Esposito, M., Mundt, R., Covino, E., Alcalá, J. M., Cusano, F., & Stecklum, B. 2007, *A&A*, 467, 1147

Guilloteau, S., & Dutrey, A. 1998, *A&A*, 339, 467

Guilloteau, S., Dutrey, A., & Simon, M. 1999, *A&A*, 348, 570

- Guilloteau, S., Dutrey, A., Pety, J., & Gueth, F. 2008, *A&A*, 478, L31
- Haisch, K. E., Lada, E. A., & Lada, C. J. 2001, *ApJ*, 553, L153
- Hamann, F., & Persson, S. E. 1992, *ApJ*, 394, 628
- Hamidouche, M., Looney, L. W., & Mundy, L. G. 2006, *ApJ*, 651, 321
- Hartmann, L., Calvet, N., Gullbring, E., & D'Alessio, P. 1998, *ApJ*, 495, 385
- Hauschildt, P. H., Allard, F., & Baron, E. 1999, *ApJ*, 512, 377
- Hawley, J. F., Gammie, C. F., & Balbus, S. A. 1995, *ApJ*, 440, 742
- Hayashi, C. 1981, *Progress of Theoretical Physics Supplement*, 70, 35
- Herbig, G. H., & Bell, K. R. 1988, in *Third Catalog of Emission Line Stars of the Orion Population* (Santa Cruz: Lick Obs.)
- Herbst, W., Herbst, D. K., & Grossman, E. J. 1994, *AJ*, 108, 1906
- Hillenbrand, L. A., & White, R. J. 2004, *ApJ*, 604, 741
- Ho, P. T. P., Moran, J. M., & Lo, K. Y. 2004, *ApJ*, 616, L1
- Hogerheijde, M. R., & van der Tak, F. F. 2000, *A&A*, 362, 697
- Hubickyj, O., Bodenheimer, P., & Lissauer, J. J. 2005, *Icarus*, 179, 415
- Hueso, R., & Guillot, T. 2005, *A&A*, 442, 703
- Hughes, A. M., Wilner, D. J., Calvet, N., D'Alessio, P., Claussen, M. J., & Hogerheijde, M. R. 2007, *ApJ*, 664, 536
- Hughes, A. M., Wilner, D. J., Qi, C., & Hogerheijde, M. R. 2008, *ApJ*, 678, 1119
- Hughes, A. M., et al. 2009, *ApJ*, submitted
- Ida, S., Larwood, J., & Burkert, A. 2000, *ApJ*, 528, 351
- Inaba, S., Wetherill, G. W., & Ikoma, M. 2003, *Icarus*, 166, 46
- Isella, A., Testi, L., Natta, A., Neri, R., Wilner, D. J., & Qi, C. 2007, *A&A*, 469, 213
- Isella, A., Carpenter, J. M., & Sargent, A. I. 2009, *ApJ*, submitted
- Johns-Krull, C. M., Valenti, J. A., & Linsky, J. L. 2000, *ApJ*, 539, 815
- Johnstone, D., Hollenbach, D., & Bally, J. 1998, *ApJ*, 499, 758

- Kenyon, S. J., & Hartmann, L. 1995, *ApJS*, 101, 117
- Kenyon, S. J., & Bromley, B. C. 2009, *ApJ*, in press (astro-ph/0811.4665)
- Kitamura, Y., Momose, M., Yokogawa, S., Kawabe, R., Tamura, M., & Ida, S. 2002, *ApJ*, 581, 357
- Koerner, D. W., & Sargent, A. I. 1995, *AJ*, 109, 2138
- Königl, A. 1991, *ApJ*, 370, L39
- Knude, J., & Høg, E. 1998, *A&A*, 338, 897
- Kuchner, M. J. 2004, *ApJ*, 612, 1147
- Kurucz, R. L. 1993, Kurucz CD-ROM 13, Atmosphere Models (Cambridge: SAO)
- Lada, C. J., & Wilking, B. A. 1984, *ApJ*, 287, 610
- Lay, O. P., Carlstrom, J. E., Hills, R. E., & Phillips, T. G. 1994, *ApJ*, 434, L75
- Lay, O. P., Carlstrom, J. E., & Hills, R. E. 1997, *ApJ*, 489, 917
- Lin, D. N. C., & Papaloizou, J. C. B. 1986, *ApJ*, 309, 846
- 1993, in *Protostars & Planets III*, eds. E. H. Levy, & J. I. Lunine (Tucson: Univ. Arizona Press), 749
- Lissauer, J. J., & Stevenson, D. J. 2007, in *Protostars & Planets V*, eds. B. Reipurth, D. Jewitt, & K. Keil (Tucson: Univ. Arizona Press), 591
- Liu, M. C., et al. 1996, *ApJ*, 461, 334
- Loinard, L., Torres, R. M., Mioduszewski, A. J., & Rodríguez, L. F. 2008, *ApJ*, 675, L29
- Lombardi, M., Lada, C. J., & Alves, J. 2008, *A&A*, 480, L785
- Lubow, S. H., Seibert, M., & Artymowicz, P. 1999, *ApJ*, 526, 1001
- Lubow, S. H., & D'Angelo, G. 2006, *ApJ*, 641, 526
- Luhman, K. L., & Rieke, G. H. 1999, *ApJ*, 525, 440
- Luu, J. X., & Jewitt, D. C. 2002, *ARA&A*, 40, 63
- Lynden-Bell, D., & Pringle, J. E. 1974, *MNRAS*, 168, 603
- Martin, P. G., & Whittet, D. C. B. 1990, *ApJ*, 357, 113
- Mathis, J. S. 1990, *ARA&A*, 28, 37



- Mayer, L., Lufkin, G., Quinn, T., Wadsley, J. 2007, *ApJ*, 661, L77
- McCabe, C., Ghez, A. M., Prato, L., Duchene, G., Fischer, R. S., & Telesco, C. 2006, *ApJ*, 636, 932
- McCaughrean, M. J., & O’Dell, C. R. 1996, *AJ*, 111, 1977
- Miyake, K., & Nakagawa, Y. 1993, *Icarus*, 106, 20
- Mundy, L. G., et al. 1996, *ApJ*, 464, L169
- Muzerolle, J., Hartmann, L., & Calvet, N. 1998, *AJ*, 116, 2965
- Natta, A., Testi, L., Neri, R., Shepherd, D. S., & Wilner, D. J. 2004, *A&A*, 416, 179
- Natta, A., Testi, L., & Randich, S. 2006, *A&A*, 452, 245
- Najita, J. R., Strom, S. E., & Muzerolle, J. 2007, *MNRAS*, 378, 369
- Nürnbergger, D., Brandner, W., Yorke, H. W., & Zinnecker, H. 1998, *A&A*, 330, 549
- Osterloh, M., & Beckwith, S. V. W. 1995, *ApJ*, 439, 288
- Padgett, D. L., et al. 2006, *ApJ*, 645, 1283
- 2008, *ApJ*, 672, 1013
- Papaloizou, J. C. B., Nelson, R. P., Kley, W., Masset, F. S., & Artymowicz, P. 2007, in *Protostars & Planets V*, eds. B. Reipurth, D. Jewitt, & K. Keil (Tucson: Univ. Arizona Press), 655
- Patience, J., Akeson, R. L., & Jensen, E. L. N. 2008, *ApJ*, 677, 616
- Piétu, V., Dutrey, A., & Kahane, C. 2003, *A&A*, 398, 565
- Piétu, V., Guilloteau, S., & Dutrey, A. 2005, *A&A*, 443, 945
- Piétu, V., Dutrey, A., Guilloteau, S., Chapillon, E., & Pety, J. 2006, *A&A*, 460, L43
- Piétu, V., Dutrey, A., & Guilloteau, S. 2007, *A&A*, 467, 163
- Pinte, C., et al. 2008, *A&A*, 489, 633
- Pollack, J. B., Hubickyj, O., Bodenheimer, P., Lissauer, J. J., Podolak, M., & Greenzweig, Y. 1996, *Icarus*, 124, 62
- Pontoppidan, K. M., Blake, G. A., van Dishoeck, E. F., Smette, A., Ireland, M. J., & Brown, J. 2008, *ApJ*, 684, 1323
- Prato, L., Greene, T. P., & Simon, M. 2003, *ApJ*, 584, 853

- Press, W. H., Teukolsky, S. A., Vetterling, W. T., & Flannery, B. P. 1992, *Numerical Recipes in FORTRAN* (2nd edition; Cambridge: Cambridge University Press)
- Pringle, J. E. 1981, *ARA&A*, 19, 137
- Raymond, S. N., Quinn, T., & Lunine, J. I. 2005, *ApJ*, 632, 670
- Rice, W. K. M., Armitage, P. J., Wood, K., & Lodato, G. 2006, *MNRAS*, 373, 1619
- Rodmann, J., Henning, T., Chandler, C. J., Mundy, L. G., & Wilner, D. J. 2006, *A&A*, 446, 211
- Scheegerer, A., Wolf, S., Voshchinnikov, N. V., Przygodda, F., & Kessler-Silacci, J. E. 2006, *A&A*, 456, 535
- Shakura, N. I., & Sunyaev, R. A. 1973, *A&A*, 24, 337
- Shu, F., Najita, J., Ostriker, E., Wilkin, F., Ruden, S., & Lizano, S. 1994, *ApJ*, 429, 781
- Shu, F. H., Galli, D., Lizano, S., Glassgold, A. E., & Diamond, P. H. 2007, *ApJ*, 665, 535
- Siess, L., Dufour, E., & Forestini, M. 2000, *A&A*, 358, 593
- Simon, M., Dutrey, A., & Guilloteau, S. 2000, *ApJ*, 545, 1034
- Stapelfeldt, K. R. 2008, private communication
- Stanke, T., Smith, M. D., Gredel, R., & Kanzadyan, T. 2006, *A&A*, 447, 609
- Stone, J. M., Hawley, J. F., Gammie, C. F., & Balbus, S. A. 1996, *ApJ*, 463, 656
- Testi, L., Natta, A., Shepherd, D. S., & Wilner, D. J. 2001, *ApJ*, 554, 1087
- Varnière, P., Blackman, E. G., Frank, A., & Quillen, A. C. 2006, *ApJ*, 640, 1110
- Vorobyov, E. I. 2008, *ApJ*, in press (astro-ph/0810.1393)
- Vorobyov, E. I., & Basu, S. 2007, *MNRAS*, 381, 1009
- 2009, *MNRAS*, in press (astro-ph/0812.1306)
- Vrba, F. J., Coyne, G. V., & Tapia, S. 1993, *AJ*, 105, 1010
- Weaver, W. B., & Jones, G. 1992, *ApJS*, 78, 239
- Weidenschilling, S. J. 1977, *Ap&SS*, 51, 153
- Weidenschilling, S. J., Spaute, D., Davis, D. R., Marzari, F., & Ohtsuki, K. 1997, *Icarus*, 128, 429
- Weingartner, J. C., & Draine, B. T. 2001, *ApJ*, 548, 296

Wetherill, G. W. 1996, *Icarus*, 119, 219

Wilking, B. A., Meyer, M. R., Robinson, J. G., & Greene, T. P. 2005, *AJ*, 130, 1733

Wilner, D. J., Ho, P. T. P., Kastner, J. H., & Rodríguez, L. F. 2000, *ApJ*, 534, L101

Wilner, D. J., D’Alessio, P., Calvet, N., Claussen, M. J., & Hartmann, L. 2005, *ApJ*, 626, L109

Youdin, A. N. 2008, in *Physics and Astrophysics of Planetary Systems* (EDP Sciences: EAS Publications Series), astro-ph/0807.111